Resonant quasiparticle-ion scattering in anisotropic superfluid ^{3}He

R. H. Salmelin and M. M. Salomaa
Low Temperature Laboratory, Helsinki University of Technology, 02150 Espoo, Finland
(Received 9 May 1989; revised manuscript received 19 September 1989)

Low-energy excitations in quantum fluids are most directly encountered by ions. In the superfluid phases of ^{3}He the relevant elementary excitations are Bogoliubov quasiparticles, which undergo repeated scattering off an ion in the presence of a divergent density of states. We present a quantum-mechanical calculation of the resonant ^{3}He quasiparticle-scattering-limited mobility for negative ions in the anisotropic bulk ^{3}He-A (A phase) and ^{3}He-P (polar phase) that is exact when the quasiparticles scatter elastically. We develop a numerical scheme to solve the singular equations for quasiparticle-ion scattering in the A and P phases. Both of these superfluid phases feature a uniaxially symmetric order parameter but distinct topology for the magnitude of the energy gap on the Fermi sphere, i.e., points versus lines of nodes. In particular, the perpetual orbital circulation of Cooper pairs in ^{3}He-A results in a novel, purely quantum-mechanical intrinsic Magnus effect, which is absent in the polar phase, where Cooper pairs possess no spontaneous orbital angular momentum. This is of interest also for transport properties of heavy-fermion superconductors. We discuss the ^{3}He quasiparticle-ion cross sections, which allow one to account for the mobility data with essentially no free parameters. The calculated mobility thus facilitates an introduction of "ion spectroscopy" to extract useful information on fundamental properties of the superfluid state, such as the temperature dependence of the energy gap in ^{3}He-A.

I. INTRODUCTION

An electron injected into liquid helium forms an electron "bubble": a cavity enclosing the electron.[1] These singly charged negative ions provide unique microscopic probes of elementary excitations in the superfluids formed by ^{4}He and ^{3}He. The low-energy excitations may be investigated with the use of ions not only in the homogeneous superfluids but also in their inhomogeneous states—such as quantized vortex lines. Here we calculate the mobility of negative ions in the anisotropic superfluid states of liquid ^{3}He that are relevant for the stationary bulk A phase and for the P (polar) phase, the proposed vortex-core matter in the rotating A phase;[2] for gap topologies, see Sec. II. The resonant scattering of the pair-correlated superfluid quasiparticles provides the drag force on ions moving in an applied electric field, $\mathcal{E}$.

The elementary excitations limiting the ionic mobility in superfluid ^{4}He (He-II) are bosons: rotons and phonons. In superfluid ^{3}He, the collective modes do not couple effectively to ionic motion, owing to their low density and long wavelength. In the superfluid phases of ^{3}He the relevant elementary excitations interacting with negative ions[3] are pair-correlated fermionic quasiparticles; this underlies the usefulness of ions as probes of the energy gap in ^{3}He. This paper discusses how ion-mobility data provide quantitative measures of superfluid properties, such as the energy gap and the Cooper-pair orbital angular momentum in ^{3}He-A.

Prior to experiments, ionic mobility in superfluid ^{3}He was expected to increase with respect to the mobility in the normal Fermi liquid.[4] However, the expression for the mobility accounted for only half the measured rise in the mobility; it was derived under the assumption of a constant differential scattering cross section, neglecting the superfluid quasiparticle dynamics, but allowing for their kinematics. To understand the experimental increase it proves crucial to recognize that, in the presence of the divergent density of states for the initial and final quasiparticles in the scattering process, there results a dynamical resonant-scattering phenomenon.[5] In the superfluid B phase, this process does not depend on the incident quasiparticle direction, $\hat{\mathbf{p}}$, on the Fermi sphere, owing to the isotropy of the energy gap, but only on the relative angle $\cos^{-1}(\hat{\mathbf{p}}\cdot\hat{\mathbf{p}}')$. However, the scattering in ^{3}He-A and ^{3}He-P is anisotropic, thus leading to a tensor structure for the ionic mobility.

Although the ^{3}He quasiparticle-ion scattering amplitude in the superfluid B phase can be obtained in closed form,[5] it evades an exact solution for the anisotropic A phase where the scattering amplitude must be obtained numerically.[6] Resonant impurity-scattering processes are relevant in other systems as well, such as heavy-fermion superconductors. Thus it proves useful to consider anisotropic quasiparticle scattering, and such new phenomena as the quantum-mechanical Magnus effect; the mathematical formulation is discussed in Sec. III.

In Sec. IV we introduce the numerical method for solving directly the singular Lippman-Schwinger equation in the case of resonant quasiparticle scattering in anisotropic pair-correlated states. Numerical results are presented in Secs. V and VI. In particular, we illustrate the evolution of the interference of several partial waves in the scattering process when the impact parameter is increased; this proves crucial for explaining the experimental mobility.

We consider two axisymmetric superfluid states, the A and P phases, which are also used as possible states of heavy-fermion superconductivity.[7,8] They are uniaxially

symmetric but differ in the *topology* of the energy gap on the Fermi surface, with nodes on points or lines, respectively (see Sec. II). Moreover, the gap nodes in ^{3}He-A are topologically "charged,"[9] whence the Cooper pairs in ^{3}He-A possess angular momentum which may be imparted in the repeated scattering process, resulting in the peculiar skew-scattering properties in ^{3}He-A discussed in Secs. V and VII; the gap nodes in ^{3}He-P are "inert": The superfluid condensate in the P state displays no inherent angular momentum.

Related calculations in p-wave-paired heavy-fermion superconductors with A- and P-like energy gaps have recently been performed by Arfi and Pethick,[8] who obtained expressions for the thermal conductivity and ultrasonic attentuation. However, since in Ref. 8 the calculation was radically simplified by exclusively considering s-wave scattering, there are important differences: The scattering matrix became a function of only the quasiparticle energy E and not the directions of the initial and final momenta, $\hat{\mathbf{p}}$ and $\hat{\mathbf{p}}'$. Nonetheless, this approximation may suffice for heavy-fermion superconductors, since the origin of multiple scattering is not yet fully understood. In ^{3}He, however, this would be inadequate: The scattering matrix is found to be a strong function of $\hat{\mathbf{p}}$ and $\hat{\mathbf{p}}'$, due to resonant scattering.

It is possible to account for the experimental mobility with calculations that allow for superfluid pairing correlations (see Sec. VII). Moreover, one can deduce parameters characterizing the superfluid A phase (see Sec. VIII); similarly, the energy gap in the superfluid A_1 phase could be extracted from possible future ion-mobility measurements with use of this work. The quantum-mechanical Magnus force may provide a way of detecting the internal angular momentum of the ^{3}He condensate.

II. STRUCTURE OF THE ENERGY GAP

The Bardeen-Cooper-Schrieffer (BCS) theory explains the superconductivity of metals.[10] For the conduction-electron gas, the conventional Cooper pairing occurs to an s state with the orbital angular momentum quantum number $L=0$ and in a spin-singlet state with the quantum number $S=0$, leading to Cooper pairs without internal degrees of freedom and with an isotropic energy gap. The BCS theory applied to the superfluidity of ^{3}He invokes anisotropic Cooper pairing, with pairs in a relative p-wave ($L=1$) spin-triplet ($S=1$) state: Anisotropic energy gaps could thus be expected.[11] This structure is reflected in the properties of the residual quasiparticle excitations. An ion moving through the superfluid experiences a drag force due to the scattering of the ^{3}He excitations. Hence the quasiparticle-limited ion mobility carries information on the superfluid order parameter.

The orbital anisotropy with $L_z\neq 0$ of superfluid ^{3}He is manifested in the anisotropic A phase, where the Cooper pairs are in the equal-spin pairing[11] state $|S_z|=1$. Therefore, a symmetry axis $\hat{\mathbf{l}}$, coinciding with the Cooper-pair orbital angular momentum, can be ascribed to the liquid. All transport properties are expressed parallel and perpendicular to this axis; we shall, moreover, discuss an additional anisotropy in the plane perpendicular to $\hat{\mathbf{l}}$. The anisotropic energy gap in the A phase is $\Delta_A(\hat{\mathbf{p}})=\Delta_A(T)e^{i\phi}\sin\theta$, where $\hat{p}$ is the quasiparticle momentum and $\Delta_A(T)$ is the temperature-dependent energy gap, see Fig. 1(a); θ is the polar angle and ϕ defines the direction of $\hat{\mathbf{p}}$ projected onto the plane perpendicular to $\hat{\mathbf{l}}$.

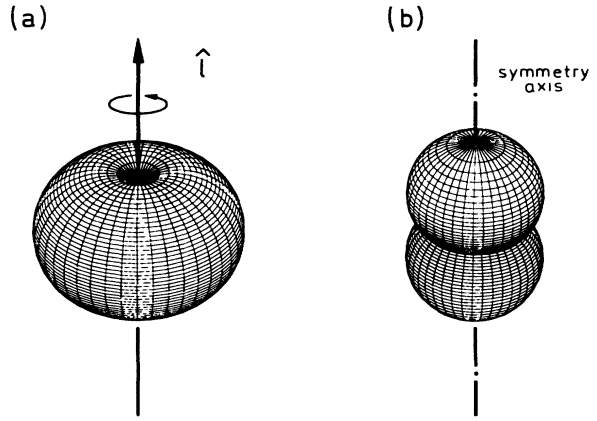

FIG. 1. Anisotropic magnitudes of the superfluid energy gap in the ABM (A) and polar (P) phases of ^{3}He. (a) In the A phase $|\Delta_A(\hat{\mathbf{p}})|=\Delta_A(T)|\sin\theta|$; thus $\Delta_A(\hat{\mathbf{p}})=0$ at two points along the direction of the angular-momentum vector $\hat{\mathbf{l}}$. (b) The P phase, in contrast, displays a line of nodes in the plane perpendicular to the symmetry axis, at the equator of the Fermi sphere, with the gap magnitude $|\Delta_P(\hat{\mathbf{p}})|=\Delta_P(T)|\cos\theta|$.

In order to illustrate the variety of effects owing to an axisymmetric energy gap, we contrast the A phase with the P phase, suggested to prevail within vortex cores in ^{3}He-A.[2] The energy gap in the P phase, where only $S_z=0, L_z=0$ Cooper pairs exist, $\Delta_P(\hat{\mathbf{p}})=\Delta_P(T)\cos\theta$, is shown in Fig. 1(b); the condensate thus possesses no intrinsic angular momentum. In contrast with $\Delta_A(\hat{\mathbf{p}})$, which vanishes only at two points on the $\hat{\mathbf{l}}$ axis, $\Delta_P(\hat{\mathbf{p}})$ exhibits a line of nodes on the equator of the Fermi sphere. This leads to important qualitative differences in the scattering of quasiparticles off an ion, to be discussed in Secs. VI and VII.

III. QUASIPARTICLE-ION MOMENTUM TRANSFER

The negative ion is a low-energy electron which, when immersed into liquid ^{3}He, forms a cavity of radius 1–2 nm around it.[1] This large "bubble" produces a huge effective hydrodynamical renormalized mass for the electron, on the order of $(100-400)m_3$, i.e., some 10^6 times the mass of an ordinary electron. The mobility of such heavy electrons remains constant in the normal Fermi liquid at all temperatures down to the superfluid transition $T=T_c$, whereafter the mobility rises rapidly in the superfluid phases as the temperature is further decreased.

The propagation of this extraordinarily heavy electron is limited only by collisions with the elementary thermal excitations at temperatures well below the Fermi temperature $T_F\approx 1$ K; in normal and superfluid ^{3}He, these are the ^{3}He quasiparticles. The first calculations were performed using a model where the ion was assumed to recoil like a free particle, leading to the limiting temperature $T_0\approx(m^*/M)T_F$, where m^* is the effective mass of a

^{3}He quasiparticle and M is the effective mass of the ion. Down to $T_0=20-100$ mK, depending on the pressure, the mobility was found to remain constant while, from T_0 downwards, the model predicted a rise $\propto T^{-2}$.[12] This effect, however, was not observed in experiments.[13] Actually, the ion does not recoil freely in collisions with quasiparticles but, owing to its continuous interaction with them, it undergoes Brownian motion. This model of Josephson and Lekner[14] sufficed to explain the constancy of the mobility down to temperatures well below T_0.

Bowley[4] extended the calculations into superfluid ^{3}He-A. The effect of the appearance of the anisotropic energy gap, which reduces the density of available initial and final scattering states and also the number of thermal excitations, was taken into account. He employed a constant cross section for those angles for which there are possible initial and final quasiparticle states. The tensor structure of the ion mobility can thus be qualitatively understood. However, the cross section is modified by the pairing correlations in an essential way. Early calculations were developed according to the Josephson-Lekner formalism: A Bogoliubov transformation on the normal-state scattering amplitude was performed,[15] and in another approach, the quasiparticle-ion cross section was assumed to be a function of the magnitude of the momentum transfer only and to be energy independent.[16]

The rapid rise[17] of the experimental ionic mobility below T_c could not, however, be quantitatively accounted for until allowance was made for the modification of intermediate scattering states by superfluidity.[5,6] The cross sections were obtained by solving the Lippman-Schwinger equation which contains all scattering channels in the process and the effect of the intermediate states as well.

In Ref. 6 the scattering equation was solved numerically for ^{3}He-A, expressing the matrix components as sums of spherical harmonic functions. This, however, required extensive mathematical manipulations and numerical computation of the complicated matrix elements. Here we seek a simpler, more versatile approach to facilitate its direct application to scattering processes in any superfluid phase, also in a magnetic field. We solve the Lippman-Schwinger equation by discretization, on a grid of values of $\mu=\cos\theta=\hat{\mathbf{p}}\cdot\hat{\mathbf{l}}$ and $\mu'=\cos\theta'=\hat{\mathbf{p}}'\cdot\hat{\mathbf{l}}$. We shall examine the theory underlying the earlier calculations[5] and point out the essential features of the new method, parts of which have been reported earlier in short form.[18,19] Numerical principles are described in Appendix A.

At low temperatures, the drift velocity $\mathbf{v}$ of an ion is limited by loss of momentum in quasiparticle-ion collisions. In diffusive motion, the recoil energy is on the order of Dq^2, where D is the ionic diffusion constant and the momentum transfer q typically equals the Fermi momentum. In the normal fluid and not too far below T_c, this is much less than the thermal energy, k_BT, and the collisions may be treated as elastic, which simplifies the calculation greatly; we thus follow the theoretical framework introduced in Refs. 5 and 6.

In limiting the analysis to low $\mathbf{v}$, we may also disregard the inelastic processes of quasiparticle pair creation and pair annihilation, which require an energy transfer $\approx 2\Delta$. These processes are negligible except close to the nodes in the energy gap, but there the relevant phase space tends to zero. This leads to a simple expression for the spectrum of possible energy transfers to the moving ion: $S_i(\mathbf{k},\omega)\approx 2\pi\delta(\omega)$, where $\omega=E_{p'}-E_p$, the difference between the final and initial quasiparticle energies; $\mathbf{k}$ is the momentum transferred.

We are thus essentially investigating modifications produced by the superfluid pairing correlations to the diffractive scattering of quasiparticles off a hard sphere. The impact parameter, $p_FR=8.45\rightarrow 8.85$ for pressures $29\rightarrow 20$ bar, requires that several partial waves are included in the calculation; they interfere with each other, creating the resonant-scattering effects which cause the observed high mobility of negative ions.

The drift velocity $\mathbf{v}$ is obtained by equating the rate of momentum transfer from the ion to the quasiparticles, $d\mathbf{P}/dt$, with the driving force supplied by the electric field, $e\mathcal{E}$. For small ionic concentrations, the liquid may be assumed to remain at rest during the propagation of an ion. The rate of momentum transfer may thus be expressed as

$$\frac{d\mathbf{P}}{dt}=n_3\sum_{\mathbf{k}}\sum_{\sigma\sigma'}\int_{-\infty}^{\infty}\frac{d\omega}{2\pi}\mathbf{k}S_3(\mathbf{k},\omega)\times S_i(-\mathbf{k},-\omega,\mathbf{v})|t_{\sigma'\sigma}(\mathbf{k},\omega,\mathbf{v})|^2 . \tag{1}$$

Above, n_3 is the ^{3}He number density. The effective squared T-matrix element $|t_{\sigma'\sigma}(\mathbf{k},\omega,\mathbf{v})|^2$ is here taken to be a function of $\mathbf{k}$, ω, and $\mathbf{v}$ only; the scattering T matrix is 2×2 in the initial- and final-state spins σ and σ'.

In normal ^{3}He and not too far below T_c, the primary density fluctuations entering $S_3(\mathbf{k},\omega)$, the equilibrium structure function for ^{3}He, are quasiparticle-quasihole pairs; collective modes have too small a density to be of importance here. Thus we may write

$$S_3(\mathbf{k},\omega)=\frac{1}{n_3}\sum_{\mathbf{pp}'}\delta_{\mathbf{p}'-\mathbf{p},\mathbf{k}}f_p(1-f_{p'})2\pi\delta(E_{p'}-E_p) . \tag{2}$$

Here $E_p=[\xi_p^2+|\Delta(\hat{\mathbf{p}})|^2]^{1/2}$ is the quasiparticle energy in the superfluid, which reduces to the quasiparticle energy in the normal fluid, $\xi_p\approx(p-p_F)v_F$, as $\Delta(\hat{\mathbf{p}})\rightarrow 0$; p_F and v_F are the Fermi momentum and velocity, respectively. The probability that the initial state is filled and the final state empty is expressed by the Fermi distribution function $f_p=1/[\exp(\beta E_p)+1]$, with $\beta=1/k_BT$.

For low electric fields, i.e., for small drift velocities, Eq. (1) is accurate to first order in $\mathbf{v}$. This is seen by noting that if the ^{3}He were also drifting with velocity $\mathbf{v}$, then $d\mathbf{P}/dt$ would vanish identically. Subtracting the equations for these two situations, setting $\mathbf{v}$ equal to zero in S_i and $|t_{\sigma'\sigma}(\mathbf{k},\omega,\mathbf{v})|^2$, averaging and using the detailed balance relations, and finally expanding to first order in $\mathbf{v}$, one finds

$$\frac{d\mathbf{P}}{dt}=\beta\pi\sum_{\mathbf{pp}'}\sum_{\sigma\sigma'}(\mathbf{p}'-\mathbf{p})[(\mathbf{p}'-\mathbf{p})\cdot\mathbf{v}]f_p(1-f_{p'})\times\delta(E_{p'}-E_p)|t_{\mathbf{p}'\sigma',\mathbf{p}\sigma}|^2 . \tag{3}$$

On equating $d\mathbf{P}/dt = e\mathcal{E}$ and further noting the definition for the mobility matrix μ,

$$v_i = \mu_{ij}\mathcal{E}_j \ , \tag{4}$$

we obtain the expression

$$e(\mu^{-1})_{ij} = \beta\pi \sum_{\mathbf{p}\mathbf{p}'} \sum_{\sigma\sigma'} (p_i' - p_i)(p_j' - p_j) f_p(1 - f_{p'}) \times \delta(E_{p'} - E_p)|t_{\mathbf{p}'\sigma',\mathbf{p}\sigma}|^2 \ . \tag{5}$$

In ^{3}He-B, with an isotropic energy gap, all directions are equal and, therefore, only the relative angle between the initial and final momenta is important. This allows for the direct analytical solution of the mobility equation, as performed in Ref. 5. In the axisymmetric situation like ^{3}He-A and ^{3}He-P, the directions of $\mathbf{p}$ and $\mathbf{p}'$ from the symmetry axis, expressed by the polar angles θ and θ', must be considered separately. In the plane perpendicular to this axis, however, all directions are indistinguishable, and the mobility only depends on $\phi' - \phi$, the relative orientation of $\mathbf{p}'$ and $\mathbf{p}$ projected onto this plane.

The magnitudes of all momenta involved can be taken equal to p_F; we may then change the sums over all directions of initial and final momenta into integrals over the Fermi surface as

$$\int d^3p/(2\pi)^3 = (p_F^2/2\pi^2) \int (\partial\mathbf{p}/\partial E_p) dE_p \int d\Omega/4\pi \ .$$

Here $\partial E_p/\partial\mathbf{p}$ is the quasiparticle group velocity, which has components both along the direction of the momentum and perpendicular to it, given by

$$(v_p)_{\parallel} = v_F \frac{[E_p^2 - |\Delta(\hat{p})|^2]^{1/2}}{E_p}$$

and

$$(v_p)_{\perp} = \frac{v_F}{2} \frac{\Delta^2(T)}{E_F E_p} \sin\theta\cos\theta$$

for the axisymmetric A and P phases. The perpendicular part is small in comparison with the component along $\mathbf{p}$, except for a negligible region where $E_p < \Delta^2(T)/E_F$.

By further noting that, on the Fermi surface,

$$f_p(1 - f_{p'}) = -(1/\beta)(\partial f/\partial E)$$

and defining $E = E_p = E_{p'}$, the mobility may be expressed as

$$e(\mu^{-1})_{ij} = n_3 p_F \int \frac{d\Omega}{4\pi} \int dE \left[-\frac{\partial f}{\partial E} \right] \sigma_{ij}(\hat{\mathbf{p}}, E) \ , \tag{6}$$

where the transport cross sections are

$$\sigma_{ij}(\hat{\mathbf{p}}, E) = \tfrac{3}{2} \int d\Omega' (\Delta\hat{\mathbf{p}}_i)(\Delta\hat{\mathbf{p}}_j) \frac{d\sigma}{d\Omega}(\hat{\mathbf{p}}', \hat{\mathbf{p}}, E) \ . \tag{7}$$

The differential cross section is defined as

$$\frac{d\sigma}{d\Omega}(\hat{\mathbf{p}}', \hat{\mathbf{p}}, E) = \left[\frac{m^*}{2\pi} \right]^2 \frac{E}{[E^2 - |\Delta(\hat{\mathbf{p}}')|^2]^{1/2}} \times \langle |t_{\hat{\mathbf{p}}'\hat{\mathbf{p}}}|^2 \rangle \frac{E}{[E^2 - |\Delta(\hat{\mathbf{p}})|^2]^{1/2}} \ , \tag{8}$$

with the branch-averaged T-matrix element

$$\langle |t_{\hat{\mathbf{p}}'\hat{\mathbf{p}}}|^2 \rangle = \tfrac{1}{2} \sum_{\sigma\sigma'} |t_{\hat{\mathbf{p}}'\sigma',\hat{\mathbf{p}}\sigma}|^2 \ . \tag{9}$$

The total cross section is given by

$$\sigma_{\text{tot}}(\hat{\mathbf{p}}, E) = \int d\Omega' \frac{d\sigma}{d\Omega'}(\hat{\mathbf{p}}', \hat{\mathbf{p}}, E) \ . \tag{10}$$

All integrations extend over those angles θ' and θ, for which there exist possible initial and final states, i.e., where $E \geq |\Delta(\hat{\mathbf{p}})|$. All angles are allowed for $E \geq \Delta$, the maximum value of the gap. At lower energies, however, a threshold appears, which confines the initial and final momenta to the cones $0 \leq \theta \leq \theta_A$ and $\pi - \theta_A \leq \theta \leq \pi$, with $\theta_A = \sin^{-1}(E/\Delta_A)$, in the A phase; in the P phase the allowed belt is $-\theta_P \leq \theta \leq \theta_P$ for $\theta_P = \cos^{-1}(E/\Delta_P)$ (see also Figs. 7 and 13).

If one were to ignore the multiple-scattering effects and perform the constant-cross-section approximation (first used by Bowley[4] in ^{3}He-A), $d\sigma/d\Omega'$ would be replaced by a constant σ. When we define that $\hat{l} \| \hat{\mathbf{z}}$ and the $\hat{\mathbf{x}}$ axis coincides with the projection of $\hat{\mathbf{p}}$ on the plane perpendicular to $\hat{l}$, the momentum transfers are given by

$$\begin{aligned}
\Delta\hat{p}_x \Delta\hat{p}_x &= \sin^2\theta + \sin^2\theta'\cos^2(\phi' - \phi) \\
&\quad - 2\sin\theta\sin\theta'\cos(\phi' - \phi) \ , \\
\Delta\hat{p}_y \Delta\hat{p}_y &= \sin^2\theta'\sin^2(\phi' - \phi) \ , \\
\Delta\hat{p}_z \Delta\hat{p}_z &= (\cos\theta' - \cos\theta)^2 \ , \\
\Delta\hat{p}_x \Delta\hat{p}_y &= -\sin\theta\sin\theta'\sin(\phi' - \phi) \\
&\quad + \sin^2\theta\cos(\phi' - \phi)\sin(\phi' - \phi) \ , \\
\Delta\hat{p}_x \Delta\hat{p}_z &= (\cos\theta - \cos\theta')\sin\theta \\
&\quad - (\cos\theta - \cos\theta')\sin\theta'\cos(\phi' - \phi) \ , \\
\Delta\hat{p}_y \Delta\hat{p}_z &= -(\cos\theta - \cos\theta')\sin\theta'\sin(\phi' - \phi) \ .
\end{aligned} \tag{11}$$

By integrating over Ω one obtains the averaged cross sections, see Refs. 6 and 19.

We calculate $\mu_{\parallel}$ and $\mu_{\perp}$ with respect to the normal-state mobility $\mu_N = e/(n_3 p_F \sigma^N)$; the normal-state transport cross section σ^N depends only on the pressure through $p_F R$ and its value is obtained in the limit $E/\Delta_A \to \infty$. The parallel mobility $\mu_{\parallel}$ is simply μ_{zz}, whereas $\mu_{\perp}$ can be calculated from the average of the momentum transfers to the indistinguishable directions x and y, i.e., from $\frac{1}{2}(\Delta\hat{p}_x \Delta\hat{p}_x + \Delta\hat{p}_y \Delta\hat{p}_y)$; the cross terms are zero in this approximation. However, μ_{xy} acquires a small nonzero value when the resonant-scattering effects on the cross sections are taken into account in Sec. IV, leading to an additional asymmetry in the scattering perpendicular to $\hat{l}$. Close to T_c, where the energy gap is small, we find the mobility components analytically by expanding $(-\partial f/\partial E)$ to first order in $z = \Delta/k_B T$ and by replacing E with $\hat{E} = E/\Delta$; for $E > \Delta$ the constant-cross-section approximation gives a constant transport cross section, and the integral is trivial. Thus, we obtain

$$\frac{\mu_N}{\mu_{\parallel,\perp}} \approx 1-\frac{z}{2}\left[1-\int_0^1 d\hat{E}\frac{\langle \sigma_{\parallel,\perp}\rangle}{\sigma^N}\right] \tag{12}$$

leading in ^{3}He-A to the approximations

$$\frac{\mu_\parallel^A}{\mu_N}=1+0.421\frac{\Delta_A(T)}{k_BT}\ ,$$
$$\frac{\mu_\perp^A}{\mu_N}=1+0.451\frac{\Delta_A(T)}{k_BT} \tag{13}$$

close to T_c.

For the P phase (Ref. 19), we obtain the linear mobilities close to T_c

$$\frac{\mu_\parallel^P}{\mu_N}=1+0.400\frac{\Delta_P(T)}{k_BT}\ ,$$
$$\frac{\mu_\perp^P}{\mu_N}=1+0.300\frac{\Delta_P(T)}{k_BT}\ . \tag{14}$$

This simple approximation, which does not take into account the multiple-scattering phenomena in superfluid ^{3}He, nevertheless shows the tensor structure due to the axisymmetric energy gap. It correctly predicts that $\mu_\parallel$ in the A phase should be lower than $\mu_\perp$, because there are more quasiparticles moving in the direction parallel to $\hat{l}$, where the energy gap has nodes, than in the perpendicular direction. However, the approximation is not quantitatively sufficient: The rapid rise of the mobility in the superfluid phases cannot be accounted for, if a BCS-type energy gap is assumed. Changes in the cross section itself, embedded in the scattering matrix T, must be included.

IV. SCATTERING MATRIX

We now solve the Lippman-Schwinger equation for the scattering matrix T. In the normal phase, with the propagator G_N and the bare potential V, it may be written as

$$T_N=V+VG_NT_N\ . \tag{15}$$

We consider all components in the Nambu space with momentum transfers $\pm\hat{\mathbf{p}}\rightarrow\pm\hat{\mathbf{p}}'$. In principle spin structure would expand the dimensions of the matrices to 4×4, but since in the A phase only equal-spin pairs $\uparrow\uparrow$ and $\downarrow\downarrow$ exist with equal amplitudes in zero field, while the P phase exhibits $\uparrow\downarrow+\downarrow\uparrow$ pairing, we may proceed using a 2×2 matrix equation describing "spinless" fermions.

The general form for the time-ordered single-particle Green's function in the Nambu space is

$$G_{\hat{\mathbf{p}}'\sigma',\hat{\mathbf{p}}\sigma}(t-t')=\begin{bmatrix}\langle T(\psi^\dagger_{\hat{\mathbf{p}}'\sigma'}(t')\psi_{\hat{\mathbf{p}}\sigma}(t))\rangle & \langle T(\psi^\dagger_{\hat{\mathbf{p}}'\sigma'}(t')\psi^\dagger_{-\hat{\mathbf{p}}\sigma}(t))\rangle \\ \langle T(\psi_{-\hat{\mathbf{p}}'\sigma'}(t')\psi_{\hat{\mathbf{p}}\sigma}(t))\rangle & \langle T(\psi_{-\hat{\mathbf{p}}'\sigma'}(t')\psi^\dagger_{-\hat{\mathbf{p}}\sigma}(t))\rangle\end{bmatrix}. \tag{16}$$

Here $\psi_{\hat{\mathbf{p}}\sigma}$ and $\psi^\dagger_{\hat{\mathbf{p}}\sigma}$ are the ^{3}He fermion field operators, which annihilate and create normal-state quasiparticles of momentum $\hat{\mathbf{p}}$ and spin σ, respectively. In the normal fluid, the propagator has the diagonal form

$$G_N(p,E)=\begin{bmatrix}(E-\xi_p)^{-1} & 0\\ 0 & (E+\xi_{-p})^{-1}\end{bmatrix}. \tag{17}$$

The interaction potential of the ion is

$$V=\begin{bmatrix}v & 0\\ 0 & -v\end{bmatrix}. \tag{18}$$

The scattering matrix in the normal state is given by

$$T_N=\begin{bmatrix}t_N(\hat{\mathbf{p}}',\hat{\mathbf{p}}) & 0\\ 0 & -t_N(-\hat{\mathbf{p}}',-\hat{\mathbf{p}})^\dagger\end{bmatrix}, \tag{19}$$

and it only depends on the directions of the initial and final momenta through $\hat{\mathbf{p}}'\cdot\hat{\mathbf{p}}$; it may, therefore, be expanded in Legendre polynomials as

$$t_N(\hat{\mathbf{p}}',\hat{\mathbf{p}})=-\frac{1}{\pi N(0)}\sum_{l=0}^{\infty}(2l+1)e^{i\delta_l}\sin\delta_l P_l(\hat{\mathbf{p}}'\cdot\hat{\mathbf{p}})\ , \tag{20}$$

where δ_l is the scattering phase shift at Fermi energy for the partial wave l. Here they are taken for a hard sphere, defined by

$$\tan\delta_l=j_l(p_FR)/n_l(p_FR)\ ;$$

j_l and n_l are, respectively, the spherical Bessel and Neumann functions of order l. The density of states at the Fermi surface is $N(0)=m^*p_F/2\pi^2$.

The Legendre polynomials may be expressed employing the spherical harmonic functions $Y_{lm}(\theta,\phi)$.[6] In the present approach we further develop the expansions: The ϕ dependence is extracted by changing the order of the sums over m and l; we denote

$$t_N(\hat{\mathbf{p}}',\hat{\mathbf{p}})=-\frac{1}{\pi N(0)}\sum_{m=-\infty}^{\infty}t_N^m(\mu',\mu)e^{-im(\phi'-\phi)}\ , \tag{21}$$

where the coefficients $t_N^m(\mu',\mu)$ are

$$t_N^m(\mu',\mu)=\sum_{l=|m|}^{\infty}\frac{2l+1}{\cot\delta_l-i}\frac{(l-|m|)!}{(l+|m|)!}\times P_l^{|m|}(\mu')P_l^{|m|}(\mu)\ . \tag{22}$$

This depends only on the direction of the initial and final momenta through $\mu=\cos\theta$ and $\mu'=\cos\theta'$, and on the pressure through the phase shifts δ_l; note also that $t_N^{-m}(\mu',\mu)=t_N^m(\mu',\mu)$. The scattering process is summed over states of definite m, corresponding to the projections of the various partial waves on the symmetry axis.

Superfluidity modifies the single-particle properties dramatically and a new ground state appears where particles and holes are coupled; this is described by the anomalous Gor'kov contractions represented by the off-diagonal terms in G_S^{-1}, proportional to Δ. We may consider an unperturbed superfluid, since the local texture is practically unmodified by the small ion;[20] we thus employ

$$G_S(\hat{\mathbf{p}},E)=\frac{1}{E^2-[\xi_p^2+|\Delta(\hat{\mathbf{p}})|^2]}\begin{bmatrix}E+\xi_{-p} & -\Delta(\hat{\mathbf{p}})\\ -\Delta^\dagger(\hat{\mathbf{p}}) & E-\xi_p\end{bmatrix}. \tag{23}$$

The bare interaction potential V in Eq. (18) is not affected by the superfluid pairing correlations. We can eliminate V in favor of T_N by combining the Lippman-Schwinger equation in the superfluid

$$T_S=V+VG_ST_S \tag{24}$$

with Eq. (15); we then obtain

$$T_S=T_N+T_N(G_S-G_N)T_S\ . \tag{25}$$

The second term in the preceding equation includes the important intermediate scattering states which modify the normal-state scattering matrix.[6] By noting that the factor G_S-G_N is small, except close to the Fermi surface, and that T_N depends strongly on momenta only for magnitudes close to p_F, we may put $|\mathbf{p}'|=|\mathbf{p}|=p_F$ in T_S and T_N. Hence the integral of G_S-G_N over the *magnitude* of the intermediate-state momentum may be factored out. The Green's function, integrated over ξ_p, is then

$$F_E(\hat{\mathbf{p}})=\begin{bmatrix}g_E(\hat{\mathbf{p}}) & f_E(\hat{\mathbf{p}})\\ f_E(\hat{\mathbf{p}}) & g_E(\hat{\mathbf{p}})\end{bmatrix}=\int\frac{p^2dp}{2\pi^2}[G_S(\hat{\mathbf{p}},E)-G_N(\hat{\mathbf{p}},E)]\ . \tag{26}$$

This energy-integrated Green's function, from which the density of quasiparticle states may be obtained, will be discussed in detail for ^{3}He-A in Sec. IV A and for ^{3}He-P in Sec. IV B.

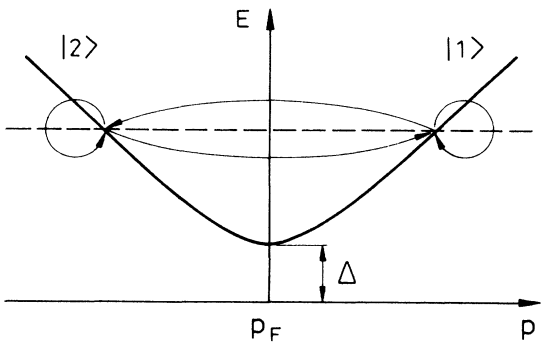

FIG. 2. Possible branches of quasiparticle dispersion relation about the Fermi momentum. The particle with energy $E>0$ may scatter elastically between the eigenstates $|1\rangle$ and $|2\rangle$, as indicated by the thin arrowed lines. A similar curve may be drawn for quasiholes, $E<0$. The maximum superfluid energy gap is denoted by Δ.

We also express the components of the T matrix in the superfluid

$$T_S=\begin{bmatrix}t_1(\hat{\mathbf{p}}',\hat{\mathbf{p}}) & t_2(\hat{\mathbf{p}}',-\hat{\mathbf{p}})\\ t_3(-\hat{\mathbf{p}}',\hat{\mathbf{p}}) & t_4(-\hat{\mathbf{p}}',-\hat{\mathbf{p}})\end{bmatrix} \tag{27}$$

as sums over m, analogously with those in the normal phase, Eq. (21);

$$t_i(\hat{\mathbf{p}}',\hat{\mathbf{p}})=-\frac{1}{\pi N(0)}\sum_{m=-\infty}^{\infty}e^{-im(\phi'-\phi)}t_i^m(\mu',\mu)\qquad i=1,2,3,4\ . \tag{28}$$

Reversing the direction of momentum, $\hat{\mathbf{p}}\rightarrow-\hat{\mathbf{p}}$, a symmetry transformation to an antipodal point on the Fermi sphere, corresponds to $\theta\rightarrow\pi-\theta$, i.e., $\mu\rightarrow-\mu$, and $\phi\rightarrow\pi+\phi$. We thus represent the T matrix in superfluid ^{3}He-A as

$$T_S=-\frac{1}{\pi N(0)}\sum_{m=-\infty}^{\infty}e^{-im(\phi'-\phi)}\begin{bmatrix}t_1^m(\mu',\mu) & \frac{\Delta(\hat{\mathbf{p}}')}{|\Delta(\hat{\mathbf{p}}')|}(-1)^m t_2^m(\mu',-\mu)\\ \frac{\Delta^\dagger(-\hat{\mathbf{p}}')}{|\Delta(-\hat{\mathbf{p}}')|}(-1)^m t_3^m(-\mu',\mu) & t_4^m(-\mu',-\mu)\end{bmatrix}, \tag{29}$$

where the ϕ dependence of the prefactors for the components t_2^m and t_3^m has been included to simplify the ensuing manipulations in solving the Lippman-Schwinger equation

$$\begin{bmatrix}t_1(\hat{\mathbf{p}}',\hat{\mathbf{p}}) & t_2(\hat{\mathbf{p}}',-\hat{\mathbf{p}})\\ t_3(-\hat{\mathbf{p}}',\hat{\mathbf{p}}) & t_4(-\hat{\mathbf{p}}',-\hat{\mathbf{p}})\end{bmatrix}=\begin{bmatrix}t_N(\hat{\mathbf{p}}',\hat{\mathbf{p}}) & 0\\ 0 & t_N^\dagger(-\hat{\mathbf{p}}',-\hat{\mathbf{p}})\end{bmatrix}+\int\frac{d\Omega''}{4\pi}\begin{bmatrix}t_N(\hat{\mathbf{p}}',\hat{\mathbf{p}}'') & 0\\ 0 & t_N^\dagger(-\hat{\mathbf{p}}',-\hat{\mathbf{p}}'')\end{bmatrix}\begin{bmatrix}g_E(\hat{\mathbf{p}}'') & f_E(\hat{\mathbf{p}}'')\\ f_E(\hat{\mathbf{p}}'') & g_E(\hat{\mathbf{p}}'')\end{bmatrix}\begin{bmatrix}t_1(\hat{\mathbf{p}}'',\hat{\mathbf{p}}) & t_2(\hat{\mathbf{p}}'',-\hat{\mathbf{p}})\\ t_3(-\hat{\mathbf{p}}'',\hat{\mathbf{p}}) & t_4(-\hat{\mathbf{p}}'',-\hat{\mathbf{p}})\end{bmatrix} \tag{30}$$

for t_1^m, t_2^m, t_3^m, and t_4^m at the quasiparticle energy E.

The integral equation for the scattering matrix has thus been reduced to depend on θ' and θ only. We can, therefore,

solve Eq. (30) directly for each m on a grid of values for μ' and μ.

The elastic scattering of the quasiparticles off an ion is a coupled-channel problem where the quasiparticle momentum may freely switch between the two branches about the Fermi momentum, $|1\rangle$ and $|2\rangle$,[6] shown in Fig. 2. They are eigenstates of the inverse propagator G_S^{-1} [Eq. (23)], and they are expressed by

$$|1(\hat{\mathbf{p}})\rangle = \begin{bmatrix} u_p \\ -v_p^\dagger \end{bmatrix} \quad \text{and} \quad |2(\hat{\mathbf{p}})\rangle = \begin{bmatrix} v_p \\ -u_p^\dagger \end{bmatrix} , \tag{31}$$

where $u_p = [\frac{1}{2}(1+\xi_p/E)]^{1/2}$ and $v_p^\dagger = [\frac{1}{2}(1-\xi_p/E)]^{1/2}\Delta^\dagger(\hat{\mathbf{p}})/|\Delta^\dagger(\hat{\mathbf{p}})|$. The quasiholes ($E<0$) could be treated analogously, but due to particle-hole symmetry we here need to consider states with $E>0$ only.

Summing over all spin states, we obtain for the branch-averaged T-matrix element[5,6] the expression

$$\begin{aligned}\langle |t_{\hat{\mathbf{p}}'\hat{\mathbf{p}}}|^2 \rangle = \tfrac{1}{4}[&|\langle 1(\hat{\mathbf{p}}')|T_S(\hat{\mathbf{p}}',\hat{\mathbf{p}})|1(\hat{\mathbf{p}})\rangle|^2 + |\langle 1(\hat{\mathbf{p}}')|T_S(\hat{\mathbf{p}}',\hat{\mathbf{p}})|2(\hat{\mathbf{p}})\rangle|^2 \\ &+ |\langle 2(\hat{\mathbf{p}}')|T_S(\hat{\mathbf{p}}',\hat{\mathbf{p}})|1(\hat{\mathbf{p}})\rangle|^2 + |\langle 2(\hat{\mathbf{p}}')|T_S(\hat{\mathbf{p}}',\hat{\mathbf{p}})|2(\hat{\mathbf{p}})\rangle|^2] .\end{aligned} \tag{32}$$

Employing the identity $u_{\hat{\mathbf{p}}} v_{\hat{\mathbf{p}}} = \Delta(\hat{\mathbf{p}})/2E$ for the superfluid coherence factors, we may define the projection matrix

$$Q(\hat{\mathbf{p}}) = |1(\hat{\mathbf{p}})\rangle\langle 1(\hat{\mathbf{p}})| + |2(\hat{\mathbf{p}})\rangle\langle 2(\hat{\mathbf{p}})| = \begin{bmatrix} 1 & -\Delta(\hat{\mathbf{p}})/E \\ -\Delta^\dagger(\hat{\mathbf{p}})/E & 1 \end{bmatrix} \tag{33}$$

to express Eq. (32) succinctly as

$$\langle |t_{\hat{\mathbf{p}}'\hat{\mathbf{p}}}|^2 \rangle = \tfrac{1}{4}\mathrm{tr}[Q(\hat{\mathbf{p}})T_S^\dagger(\hat{\mathbf{p}},\hat{\mathbf{p}}')Q(\hat{\mathbf{p}}')T_S(\hat{\mathbf{p}}',\hat{\mathbf{p}})] . \tag{34}$$

All the angle- and energy-dependent resonant-scattering phenomena relevant to explaining the mobility of negative ions are incorporated in the squared scattering amplitude $\langle |t_{\hat{\mathbf{p}}'\hat{\mathbf{p}}}(E)|^2 \rangle$. This branch-averaged effective squared transition-matrix element will now be considered for the two axisymmetric ^{3}He phases with different gap structures to investigate the qualitative differences in their resonant features.

A. ^{3}He-A

The superfluid A phase is found in liquid ^{3}He just below $T_c \approx 3$ mK at pressures exceeding $p=20$ bar in zero magnetic field; at fields $H>0.6$ T, the A phase extends all the way to $T=0$. The gap matrix in zero magnetic field is given in spin space as

$$\Delta_A(\hat{\mathbf{p}}) = \Delta_A \sin\theta e^{i\phi} \begin{bmatrix} 1 & 0 \\ 0 & 1 \end{bmatrix} ; \tag{35}$$

above, Δ_A is the maximum value of the gap at a temperature T, see Figs. 1, 12, and 13. The diagonal structure allows dropping the spin indices and treating the preceding matrix as a scalar.

According to Eq. (29), we then obtain for the scattering matrix in ^{3}He-A

$$T_S(\hat{\mathbf{p}}',\hat{\mathbf{p}}) = -\frac{1}{\pi N(0)} \sum_{m=-\infty}^{\infty} e^{-im(\phi'-\phi)} \begin{bmatrix} t_1^m(\mu',\mu) & e^{i\phi'}(-1)^m t_2^m(\mu',-\mu) \\ e^{-i\phi'}(-1)^{m+1} t_3^m(-\mu',\mu) & t_4^m(-\mu',-\mu) \end{bmatrix} . \tag{36}$$

The components of the matrix $F_E(\hat{\mathbf{p}})$ in Eq. (26) are given as

$$g_E(\hat{\mathbf{p}}) = \frac{E}{(E^2-\Delta_A^2\sin^2\theta)^{1/2}} - 1 , \tag{37}$$

$$f_E(\hat{\mathbf{p}}) = -\frac{\Delta_A \sin\theta}{(E^2-\Delta_A^2\sin^2\theta)^{1/2}} e^{i\phi} , \tag{38}$$

for $E>|\Delta_A(\hat{\mathbf{p}})|$; at lower quasiparticle energies, where $E<|\Delta_A(\hat{\mathbf{p}})|$ except close to the nodes, the branch for the denominator in the above formula is to be chosen as $i(\Delta_A^2\sin^2\theta - E^2)^{1/2}$ for these virtual scattering states. The Lippman-Schwinger equation (25) is now expressed as a pair of coupled equations (A1); their numerical solution is discussed in Appendix A.

Integrating $F_E(\hat{\mathbf{p}})$ over all directions on the Fermi surface, the off-diagonal terms are found to vanish, while the diagonal elements yield

$$\rho_A(E) - \rho_N = -i\pi N(0) \times \begin{cases} (\hat{E}/2)\ln[(\hat{E}+1)/(\hat{E}-1)] - 1 , & E>\Delta_A \\ (\hat{E}/2)\ln[(1+\hat{E})/(1-\hat{E})] - i\pi(\hat{E}/2) - 1 , & E<\Delta_A , \end{cases} \tag{39}$$

where the normalized energy $\hat{E} = E/\Delta_A$. The real and imaginary parts of the density of quasiparticle states are ob-

tained as $N^A(E)=-(1/i\pi)\rho_A(E)$. This factor describes the density of intermediate states in the scattering process; the divergence of $N^A(E)$ at $E=\Delta_A$ is responsible for the vital importance of superfluid pairing correlations.

B. ^{3}He-P

The P phase is not encountered in a homogeneous superfluid ^{3}He. It may, however, occur in the inhomogeneous states, such as inside the core of an A-phase vortex.[2] Here, for simplicity, we study the uniform bulk situation, which may provide a working first approximation to the situation in A-phase vortex-core matter, see Ref. 19.

The lack of ϕ dependence in the gap matrix,

$$\Delta_P(\hat{\mathbf{p}})=\Delta_P\cos\theta\begin{bmatrix}0 & 1\\ 1 & 0\end{bmatrix}, \tag{40}$$

leads to a more symmetric resonance process than in the A phase. Here again, as in ^{3}He-A, the antidiagonal structure of the gap in spin space simplifies the problem and allows us to treat $\Delta_P(\hat{\mathbf{p}})$ as a scalar.

The scattering matrix in the P phase is represented as

$$T_S(\hat{\mathbf{p}}',\hat{\mathbf{p}})=-\frac{1}{\pi N(0)}\sum_{m=-\infty}^{\infty}e^{-im(\phi'-\phi)}\begin{bmatrix}t_1^m(\mu',\mu) & (-1)^m t_2^m(\mu',-\mu)\\ (-1)^m t_3^m(-\mu',\mu) & t_4^m(-\mu',-\mu)\end{bmatrix}. \tag{41}$$

Integration of the matrix components in $F_E(\hat{\mathbf{p}})$

$$g_E(\hat{\mathbf{p}})=\frac{E}{(E^2-\Delta_P^2\cos^2\theta)^{1/2}}-1, \tag{42}$$

$$f_E(\hat{\mathbf{p}})=-\frac{\Delta_P\cos\theta}{(E^2-\Delta_P^2\cos^2\theta)^{1/2}} \tag{43}$$

over the Fermi surface yields nonzero values for the diagonal elements only, and we find

$$\rho_P(E)-\rho_N=-i\pi N(0)\times\begin{cases}\hat{E}\sin^{-1}(1/\hat{E})-1, & E>\Delta_P,\\ (\hat{E}/2)\pi-i(\hat{E}/2)\ln\{[(1-\hat{E}^2)^{1/2}+1]/[(1-\hat{E}^2)^{1/2}-1]\}-1, & E<\Delta_P,\end{cases} \tag{44}$$

with $\hat{E}=E/\Delta_P$ for the density of quasiparticle states; $N^P(E)=-(1/i\pi)\rho_P(E)$. The superfluid T_S matrix is found by solving Eqs. (A2).

V. DIFFERENTIAL CROSS SECTION

Owing to the size of the negative ion, the impact parameter $p_FR\gg1$ and one must include several partial waves to correctly describe the scattering process in the normal state. Hence the differential cross section in Eq. (8) is far from being a constant, as it would be for pure s-wave scattering, with $p_FR\ll1$. The effect of the pairing correlations in a specific superfluid phase are incorporated in the effective squared T-matrix element, whose detailed expressions in the A and P phases are given in Appendix B.

Figures 3 show the differential scattering cross section $d\sigma/d\Omega$ [Eq. (8)] for ^{3}He-A in units of πR^2 in the plane of the incident quasiparticle momentum $\hat{\mathbf{p}}$, approximately parallel to $\hat{\mathbf{l}}$, for several values of the quasiparticle energy and the impact parameter. Below the limit set by the maximum of the superfluid energy gap, forbidden regimes appear in the spectrum (see Fig. 13). For $p_FR>1$, see Figs. 3(a)–3(c), the diminishing of the cross sections in the directions perpendicular to $\hat{\mathbf{l}}$ is obvious. This is where the effect of the superfluid energy gap is first felt as a reduction in the number of possible scattering states; this already commences above the gap edge. The forward scattering is enchanced, while the backward scattering becomes smaller until a strong backward peak is also observed for E well below Δ_A. The effect of a varying angle between $\hat{\mathbf{p}}$ and $\hat{\mathbf{l}}$ is illustrated in Fig. 3(b). The graphs are calculated just above the gap edge, where the effects of superfluidity are already clearly visible; symmetric curves (in the θ plane) with respect to $\hat{\mathbf{p}}$ are only obtained for the cases $\hat{\mathbf{p}}\parallel\hat{\mathbf{l}}$ and $\hat{\mathbf{p}}\perp\hat{\mathbf{l}}$.

With decreasing p_FR, fewer partial waves are important in the scattering process, and a smoother differential cross section is obtained. The radical change in the behavior of $d\sigma/d\Omega$ at $p_FR<1$ is obvious from Fig. 3(d), for $p_FR=0.5$; almost only the s wave interacts with the negative ion, and the cross section now becomes enhanced in the plane perpendicular to $\hat{\mathbf{l}}$.

The corresponding graphs for the polar phase are illustrated in Figs. 4, where the incident quasiparticle moves close to the line of nodes of the energy gap, see Fig. 1, almost perpendicular to the symmetry axis. These scattering cross sections of the two axisymmetric states are qualitatively very similar in the θ plane, except that the backward scattering is less prominent in the P phase.

In the plane perpendicular to the symmetry axis the scattering cross sections only depend on the angle between the projections of the incident and scattered quasiparticle momenta, $\phi'-\phi$. In the A phase the sign of the angle also becomes relevant, owing to the ϕ dependence

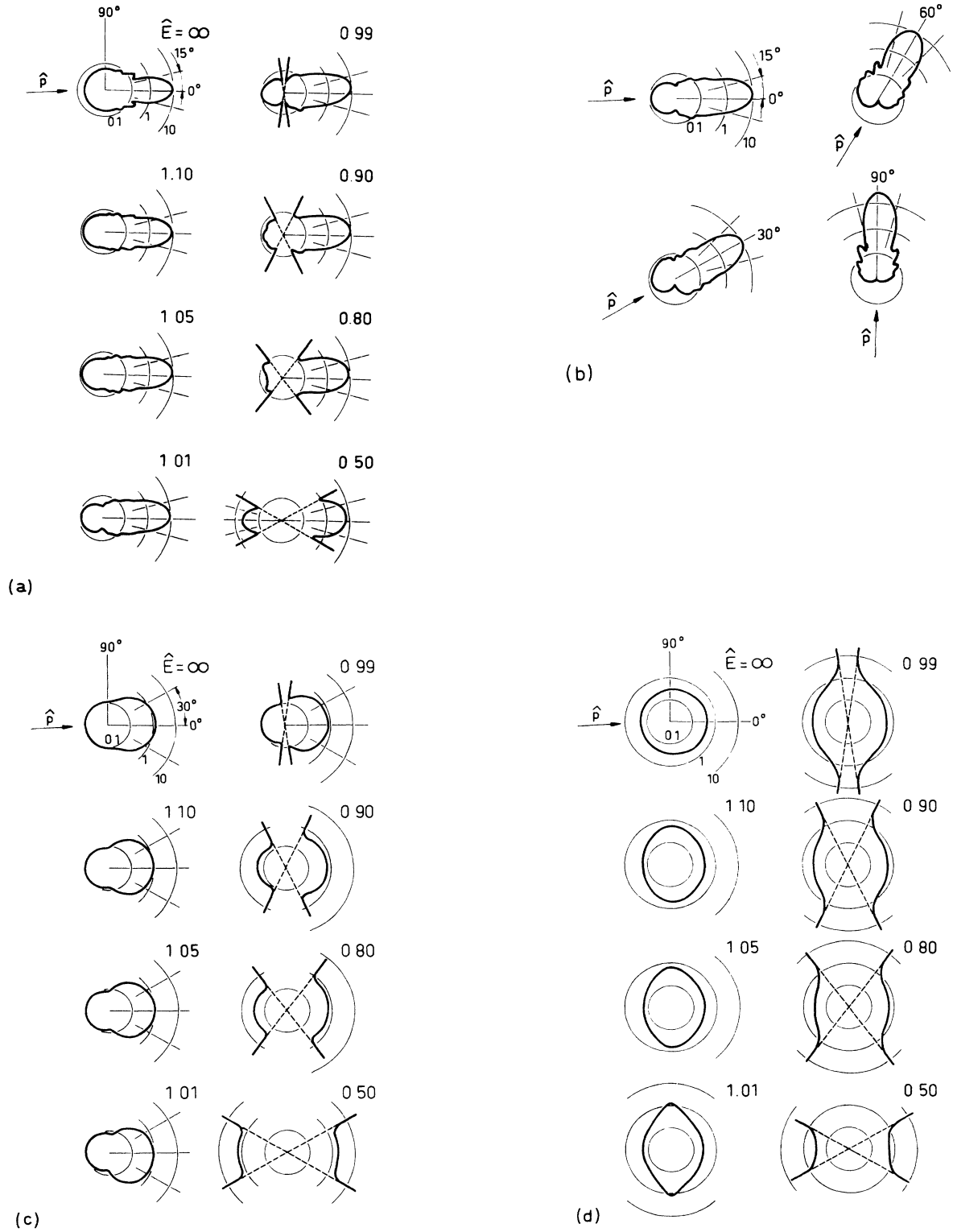

FIG. 3. Differential cross sections in ^{3}He-A (in units of πR^2) for various values of the impact parameter; the quasiparticle energies $\hat{E}=E/\Delta_A$ are indicated on the figures. The initial quasiparticle is marked with $\hat{\mathbf{p}}$. The function shows the probability amplitude into the final quasiparticle directions $\hat{\mathbf{p}}'$ in the θ plane. (a) For $p_F R=8.45$ there is a strong forward scattering peak. The backward scattering becomes strongly enhanced well below the gap edge, $\hat{E}=1$. (b) Dependence of the differential cross section on the angle between the direction of $\hat{\mathbf{p}}$ and $\hat{\mathbf{l}}$ for $p_F R=8.45$ and $\hat{E}=1.01$. Note the strong reduction of the scattering amplitude in the directions of the maximum energy gap, perpendicular to $\hat{\mathbf{l}}$. (c) For $p_F R=2.0$ the graphs become smoother as a result of interferences between fewer partial waves. (d) The radical change at $p_F R\approx 1$ is seen in these graphs which are calculated for $p_F R=0.5$. The impurity is so tiny that the s wave is only relevant; in this case the scattering is strongly enhanced in the directions of the maximum gap. Thus the effect important for large objects is qualitatively opposite for small objects.

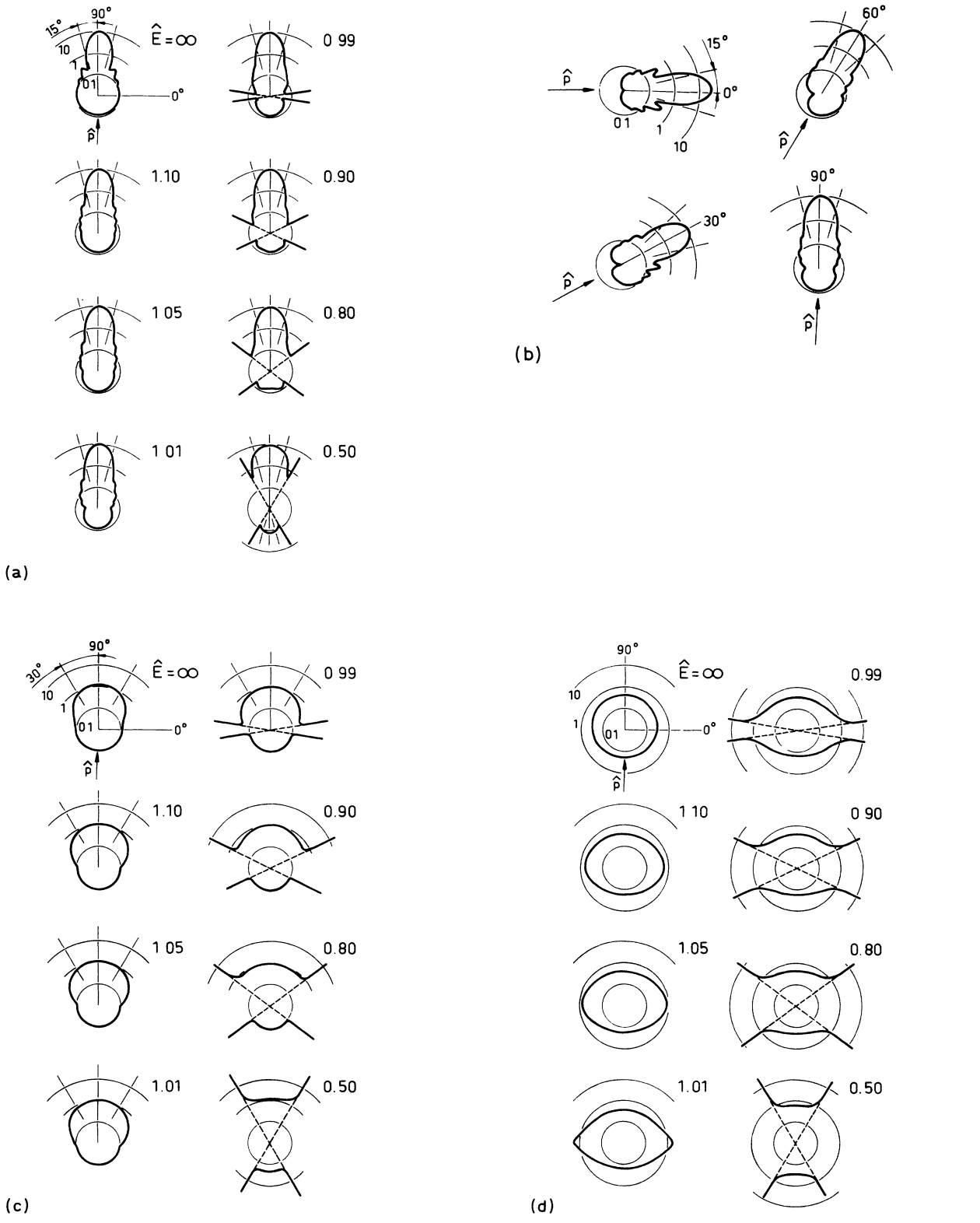

FIG. 4. Differential cross sections in ^{3}He-P for various values of the impact parameter; the quasiparticle energies $\hat{E}=E/\Delta_P$ are indicated on the figures, as in Fig. 3. (a) For $p_FR=8.45$ there is a strong forward scattering peak as in the A phase. The backward scattering becomes slightly enhanced well below the gap edge. (b) Dependence of the differential cross section on the angle θ of the incident quasiparticle for $p_FR=8.45$ and $\hat{E}=1.01$. Note the strong reduction along the symmetry axis, in the directions of the maximum energy gap. (c) For $p_FR=2.0$ the graphs become smoother as a result of interferences between fewer partial waves. (d) With $p_FR=0.5$, there is a clear change with respect to $p_FR>1$, as in ^{3}He-A. Here the scattering is strongly enhanced in the directions of the maximum gap.

of the energy gap, incorporating the effect of the nonzero L_z. In Fig. 5(a), the differential cross section for $p_F R = 8.45$ is plotted as a function of $\phi' - \phi$ for various angles θ of the incident quasiparticle momentum with respect to $\hat{l}$; note the increasing reflection asymmetry, with respect to $\hat{\mathbf{p}}$, on approaching $\hat{\mathbf{p}} \perp \hat{l}$. Fig. 5(b) illustrates the effect of the impact parameter on the maximal asymmetry; the increasing number of partial waves involved is clearly observable. In contrast, the conserved reflection symmetry in the P phase, where the directions $+(\phi' - \phi)$ and $-(\phi' - \phi)$ are indistinguishable, is evident in Fig. 5(c).

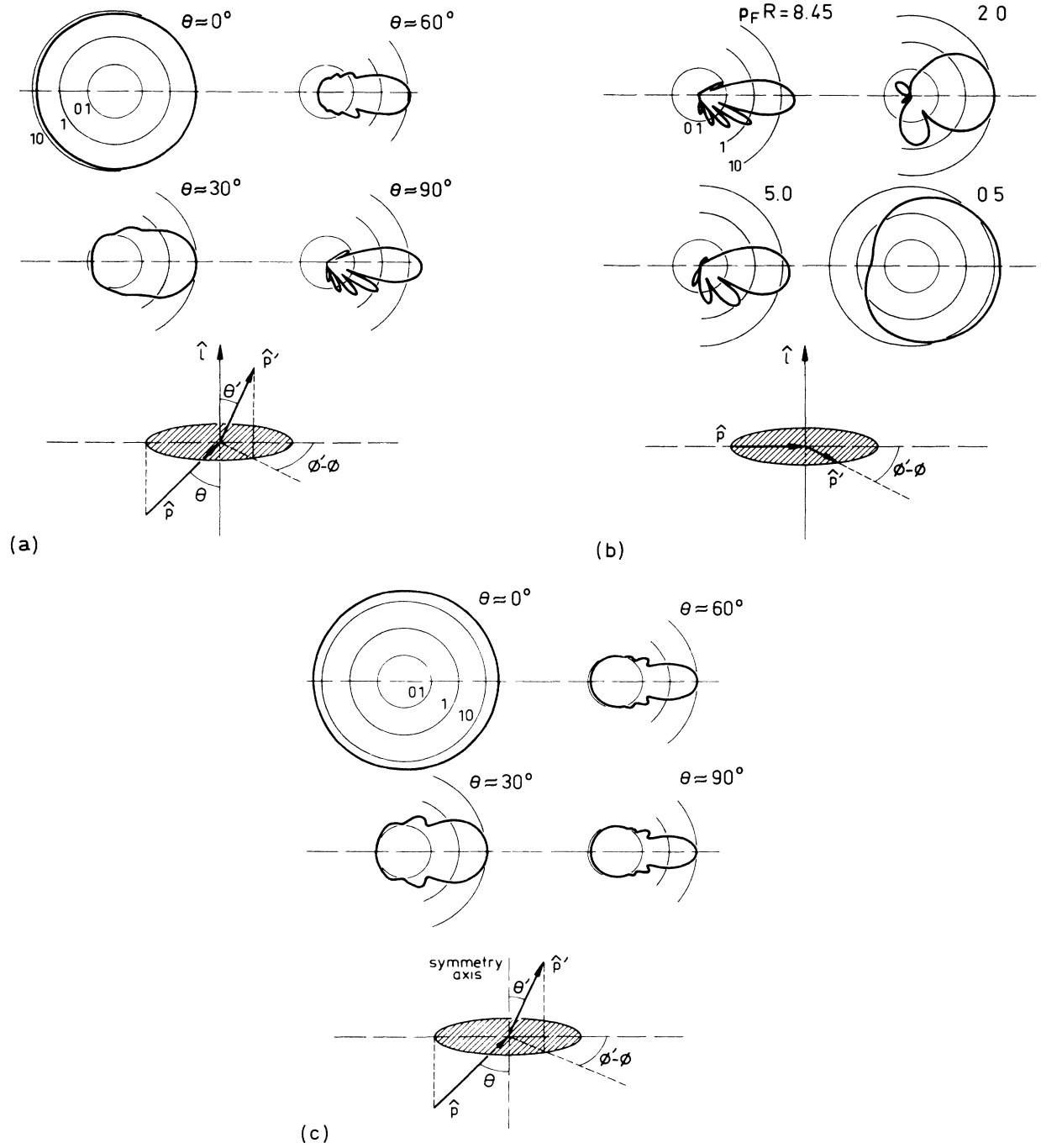

FIG. 5. Differential cross sections as functions of the relative orientation $\phi' - \phi$ of the initial ($\hat{\mathbf{p}}$) and final ($\hat{\mathbf{p}}'$) momenta on the plane perpendicular to the symmetry axis; here $\theta' = \theta$. (a) In ^{3}He-A, for $p_F R = 8.45$, just above the gap edge, $\hat{E} = 1.01$, no difference is observed in the scattering to the directions $+(\phi' - \phi)$ and $-(\phi' - \phi)$, when $\hat{\mathbf{p}} \| \hat{l}$. However, for $\theta \neq 0°$, a reflection asymmetry arises which reaches its maximum for $\hat{\mathbf{p}} \perp \hat{l}$. (b) Dependence of the maximal asymmetry in ^{3}He-A as a function of the impact parameter $p_F R$, i.e., of the number of relevant partial waves in the scattering process. This asymmetry is responsible for the Magnus-like effect for ion motion in ^{3}He-A. For $p_F R \ll 1$, the regime of pure s-wave scattering is approached, where the directions $\pm(\phi' - \phi)$ become equal. (c) For comparison, the symmetric scattering in ^{3}He-P is shown for various angles θ, at $\hat{E} = 1.01$ and $p_F R = 8.45$.

VI. CROSS SECTIONS

To find the scattering cross sections in Eqs. (7) and (10), and finally the mobilities in Eq. (5), we now calculate the integrals

$$\int d\phi' \int d\phi (\Delta\hat{\mathbf{p}}_i)(\Delta\hat{\mathbf{p}}_j)\langle |t_{\hat{\mathbf{p}}'\hat{\mathbf{p}}}|^2\rangle \ ;$$

we may then insert the T-matrix components, given by the Lippman-Schwinger equation and solved for a grid of μ' and μ. For this purpose, we express the ϕ dependence of the momentum transfers using the $\exp[\pm i(\phi'-\phi)]$ form, and evaluate the functions

$$\begin{aligned}
A(\mu',\mu) &= \int_0^{2\pi} d(\phi'-\phi)\langle |t_{\hat{\mathbf{p}}'\hat{\mathbf{p}}}|^2\rangle \ , \\
B^+(\mu',\mu) &= \int_0^{2\pi} d(\phi'-\phi) e^{i(\phi'-\phi)}\langle |t_{\hat{\mathbf{p}}'\hat{\mathbf{p}}}|^2\rangle \ , \\
B^-(\mu',\mu) &= \int_0^{2\pi} d(\phi'-\phi) e^{-i(\phi'-\phi)}\langle |t_{\hat{\mathbf{p}}'\hat{\mathbf{p}}}|^2\rangle \ , \qquad (45) \\
C^+(\mu',\mu) &= \int_0^{2\pi} d(\phi'-\phi) e^{i2(\phi'-\phi)}\langle |t_{\hat{\mathbf{p}}'\hat{\mathbf{p}}}|^2\rangle \ , \\
C^-(\mu',\mu) &= \int_0^{2\pi} d(\phi'-\phi) e^{-i2(\phi'-\phi)}\langle |t_{\hat{\mathbf{p}}'\hat{\mathbf{p}}}|^2\rangle \ .
\end{aligned}$$

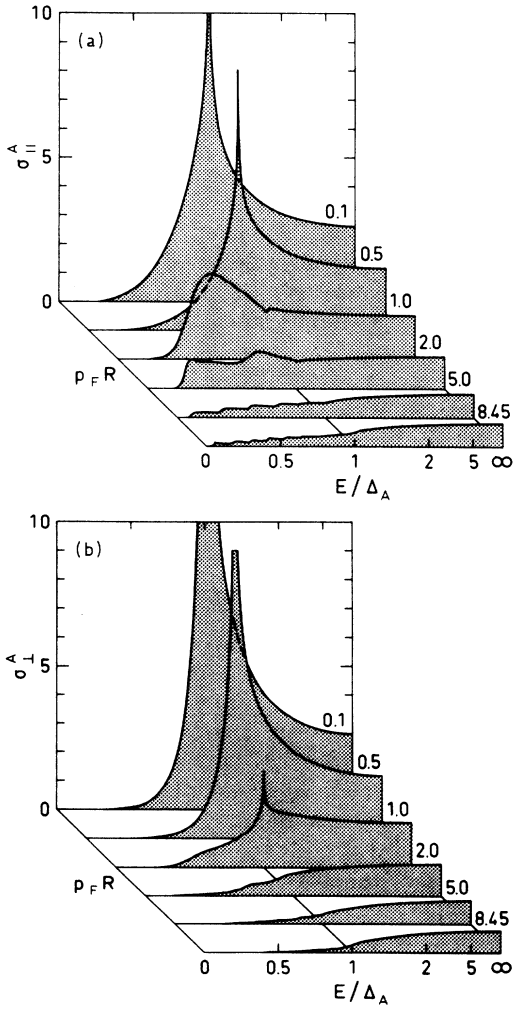

FIG. 6. Transport cross section of the quasiparticle-negative-ion scattering (a) along $\hat{l}$ and (b) in the plane perpendicular to $\hat{l}$ in ^{3}He-A in units of πR^2, plotted vs quasiparticle energy for several values of the pressure-dependent impact parameter $p_F R$, indicated on the graphs.

Their detailed forms for the A and P phases are given in Appendix B, together with the expressions for the averaged cross sections. In the A phase, $B^-(\mu',\mu)=[B^+(\mu',\mu)]^*$ and $C^-(\mu',\mu)=[C^+(\mu',\mu)]^*$, while in the more symmetric polar phase $B^-(\mu',\mu)=B^+(\mu',\mu)$ and $C^-(\mu',\mu)=C^+(\mu',\mu)$ are real. A dependence on the quasiparticle energy E is brought into these matrices by the effective T-matrix element $\langle |t_{\hat{\mathbf{p}}'\hat{\mathbf{p}}}|^2\rangle$.

A. Cross sections in the A phase

Figure 6(a) illustrates the transport cross section along the symmetry axis, $\langle \sigma_{zz}(E)\rangle$, for several values of the impact parameter $p_F R$, while the average transport cross section in the plane perpendicular to the symmetry axis, $\frac{1}{2}[\langle \sigma_{xx}(E)\rangle + \langle \sigma_{yy}(E)\rangle]$, is plotted in Fig. 6(b). The off-diagonal components are small with respect to the principal components.[21] The large range of impact parameters serves to illustrate the effect of the increasing number of partial waves involved in the resonant-scattering process.

When the size of the ion grows towards lower pressures, the interaction of the ion with more and more partial waves becomes important, which results in the overall decrease of the transport cross sections. The nodes in the energy gap are on the symmetry axis $\hat{l}$, and the ion thus experiences more quasiparticle collisions in this direction than in the plane perpendicular to $\hat{l}$, where the gap is at its maximum and effectively restricts the number of possible momentum transfers. This leads to a larger cross section and lower mobility parallel to $\hat{l}$ than in the perpendicular direction. In the limit of the isotropic normal state, $E/\Delta_A \to \infty$, the transport cross sections in Figs. 6(a) and 6(b) become constant and equal.

The nontrivial mixing of the adjacent partial waves in the A phase in the immediate vicinity of the ion gives rise to virtual resonant energy levels inside the gap, see Fig. 7(a). Since there are also real scattering states down to

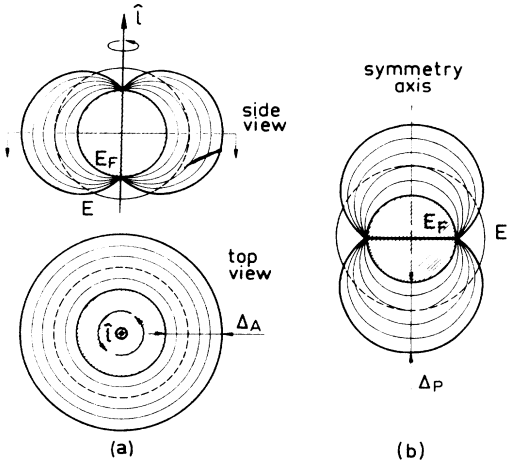

FIG. 7. Virtual energy levels created within the superfluid energy gap in the vicinity of a negative ion (a) in the A phase, including the cross-sectional view, and (b) on the P phase. An incident quasiparticle energy E, matching one of the quasi-bound states, is also shown.

$E=0$ close to the nodes, the virtual states only have a finite lifetime. When a quasiparticle has an energy matching one of these levels, it resides longer close to the ion and high momentum transfers on the order of $2p_F$ may occur, increasing the cross section. The number of resonances is roughly equal to p_FR, the number of relevant partial waves. The stepwise structure can most readily be seen in $\sigma_{\parallel}^{A}$. When $E\rightarrow 0$ the cross sections tend to vanish, as the phase space rapidly decreases in proportion to the area of cones surrounding the nodes in the energy gap.

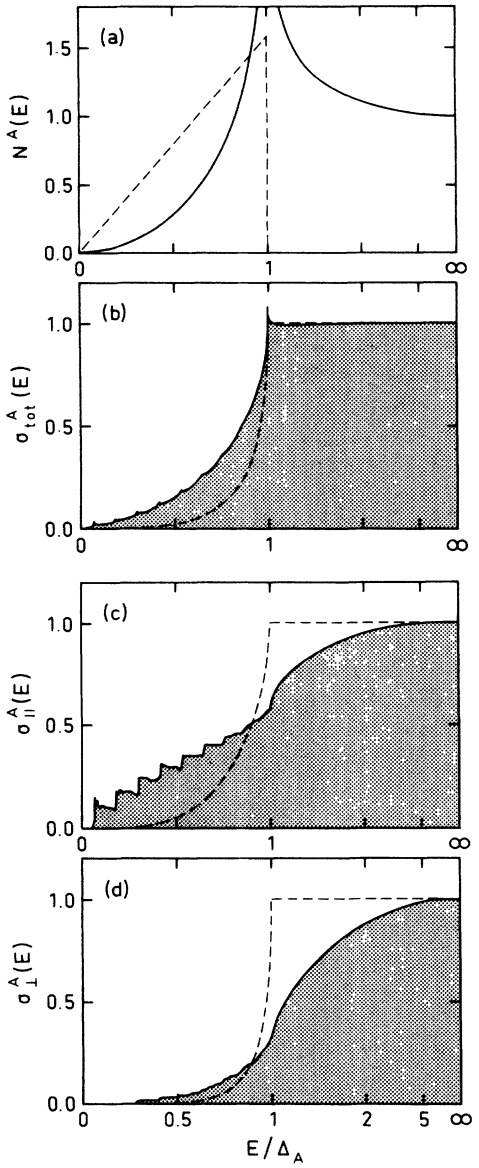

FIG. 8. Density of quasiparticle states in ^{3}He-A is featured in (a); the dashed curve is the real part while the solid curve indicates the imaginary part. In (b) through (d) the total scattering cross section and the transport cross sections along $\hat{l}$ and in the plane perpendicular to it, respectively, are illustrated for $p_FR=8.45$, corresponding to a pressure of 29 bars, in units of the normal-state value. The stepwise structure arises from the resonant energy levels within the superfluid gap, depicted in Fig. 7.

The cross sections for the experimentally relevant value $p_FR=8.45$, corresponding to 29 bar, are plotted separately in Fig. 8 for the A phase. In Fig. 8(a) the density of states, Eq. (39), is seen to diverge close to the gap edge; this is the reason for the failure of the Born approximation to solve the scattering matrix. The structure of N^A is responsible for the discontinuity observable in the cross sections at $E=\Delta_A$.

The constant-cross-section approximation,[4,6] is depicted in Figs. 8(b)–8(d) by dashed curves. It predicts a constant normal-state value down to the gap edge, where an abrupt decrease is obtained. We find that the cross sections are already affected by the anisotropic gap well above $E=\Delta_A$, leading to a greatly reduced perpendicular transport cross section and, hence, to an increased mobility with respect to the simplified approach. This appears to be in good agreement with the experiments done in ^{3}He-A.[17]

The cross sections for the A phase at $p_FR=8.45$ have also been calculated in Ref. 6, employing the properties of the spherical harmonic functions. The results do agree qualitatively with this work, showing a similar step structure and decrease of the transport cross sections above the gap edge. Quantitatively, however, there are some differences, most notably a sharp zero-going peak in $\sigma_{\parallel}^{A}$ in the earlier work at the gap edge, which we do not see in our direct method of solving the Lippman-Schwinger equation. We are inclined to relate the result found in Ref. 6 to possible numerical instabilities in the Clebsch-Gordan coefficients and the spherical harmonics close to $E=\Delta_A$, because of the divergence in the density of quasiparticle states; in our approach, this difficulty has been effectively taken care of, see Appendix A for numerical methods.

B. Cross sections in the P phase

The corresponding results for the polar phase are displayed in Fig. 9. Even though the differential cross sections of the A and P phases, Figs. 3 and 4, are very similar, a clear qualitative difference is observed in the averaged cross sections. The absence of resonance energies in the P-phase graphs would suggest that here the virtual energy levels do not support such large momentum transfers as in the A phase, due to the belt of nodes, which divides the energy gap strictly to two separate hemispheres and makes the energy levels dispersive in all directions, see Fig. 7(b).

In this case, the major momentum transfers down to the lowest quasiparticle energies occur on the equator, and we thus find that $\sigma_{\perp}^{P}>\sigma_{\parallel}^{P}$, leading to higher ionic mobility along the symmetry axis than in the plane perpendicular to it. The large feature, moving towards lower energies with increasing p_FR, observed in Fig. 9(b) for $\sigma_{\perp}^{P}$ in particular, is related to an accumulation of resonant quasibound states and the backscattering for the differential cross section (see Fig. 4), which appears at low energies and temporarily increases the cross section due to the large momentum transfers, approximately $2p_F$. When the energy decreases further, the spectral weight of this effect finally reduces to zero.

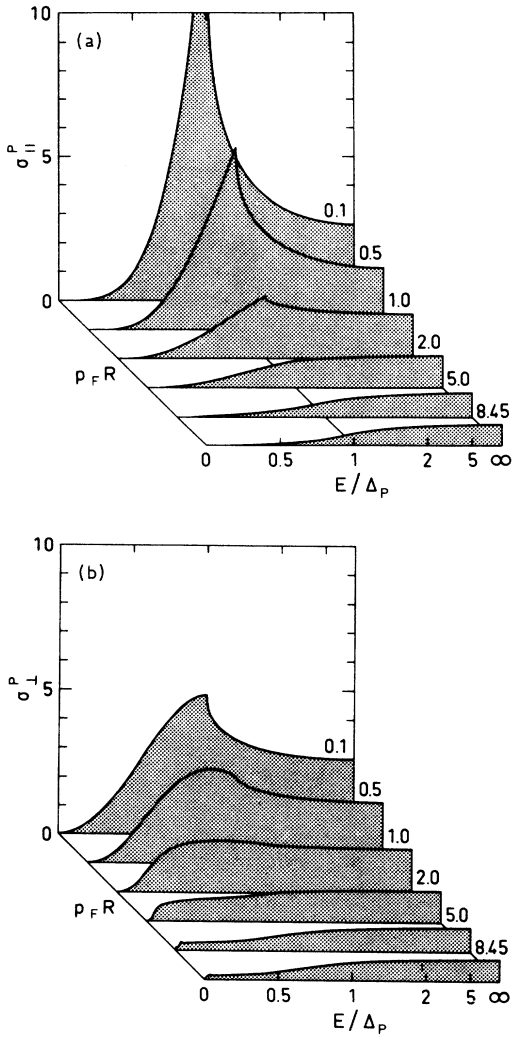

FIG. 9. Transport cross section of the quasiparticle-negative-ion scattering (a) along the symmetry axis in ^{3}He-P and (b) perpendicular to it in units of πR^2, plotted vs quasiparticle energy for several values of the impact parameter $p_F R$.

There is no divergence in the density of states for quasiparticles in the P phase,[19] and the cross sections do not show discontinuities close to the gap edge. The constant-cross-section approximation is found quite insufficient in this case as well. These results have recently been employed to estimate the mobility of ions in an A-phase vortex with polar core.[19]

Nonzero values of the cross terms $\langle\sigma_{xy}(E)\rangle$, $\langle\sigma_{xz}(E)\rangle$, and $\langle\sigma_{yz}(E)\rangle$ would indicate a deflecting force on the ion propagating in the corresponding plane. As expected, the cross sections in the indistinguishable planes xz and yz equal zero in both phases, due to the antisymmetric prefactor $(\mu'-\mu)$ in the integrand. So does the xy component in the P phase, where the $B^{\pm}(\mu',\mu)$ matrices are real and equal, as well as the $C^{\pm}(\mu',\mu)$ matrices. In the A phase, however, a nonzero $\langle\sigma_{xy}(E)\rangle$ is obtained at energies close to the gap edge.[21]

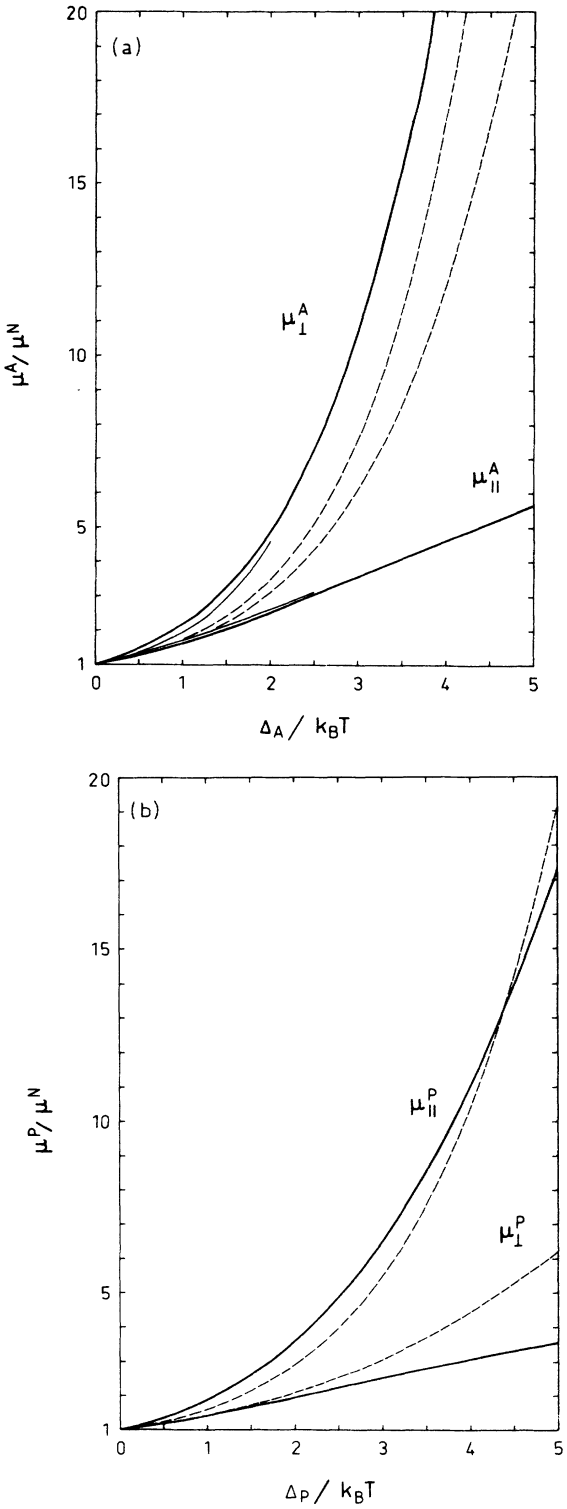

FIG. 10. (a) Calculated mobilities in ^{3}He-A as functions of the maximum energy gap, essentially the only free parameter. The thick curves were obtained from the present calculation, while the short thin ones are the results from Ref. 6 where similar assumptions but different methods were employed to find the mobilities; the dashed curves indicate the value found in the constant-cross-section approximation (Bowley, Ref. 4). (b) The solid curves are the mobilities in ^{3}He-P found in the present calculation, while the dashed lines indicate the results obtained in the constant-cross-section approximation.

VII. RESULTS FOR THE MOBILITY

The parallel and perpendicular mobilities in the A phase are plotted in Fig. 10(a) normalized to the normal-state value for $p_F R = 8.45$; the earlier calculations[6] and the constant-cross-section results[4] are also included. Close to T_c we find

$$\frac{\mu_\parallel^A}{\mu^N} = 1 + 0.532 \frac{\Delta_A(T)}{k_B T} ,$$
$$\frac{\mu_\perp^A}{\mu^N} = 1 + 0.727 \frac{\Delta_A(T)}{k_B T} . \tag{46}$$

The difference from the Bowley approximation is found to be largest in the perpendicular mobility as could be expected on comparing the cross sections.

In the A phase, there appears skew scattering in the xy plane, which leads to an essentially quantum mechanical, Magnus-like effect (Ref. 21); the well-known classical Magnus force is observed in a situation where a rotating object travels in a viscous fluid. This is illustrated in Fig. 11(a), in a coordinate system where the object is at rest while the liquid flows past it at a velocity $\mathbf{v}$; the circulation of the body is $\boldsymbol{\kappa}$. On the right-hand side the circulation opposes the velocity, while on the opposite side the two flows reinforce one another. According to the Bernoulli equation, the liquid exerts a higher pressure on the object at right, resulting in a net reactive force which tends to deflect the body from its original trajectory, in the direction perpendicular to both $\hat{\boldsymbol{\kappa}}$ and $\hat{\mathbf{v}}$; this is known as the Magnus force $\mathbf{F}_M \propto \boldsymbol{\kappa} \times \mathbf{v}$.

In the analogous quantum effect suggested[21] to occur in ^{3}He-A the roles of the object and the medium are found to be reversed: The superfluid itself has an internal orbital angular momentum $\hat{l}$, a coherent property of all the condensate interacting with the ion, see Fig. 11(b). Because of the lack of reflection symmetry in the scattering process in the plane perpendicular to $\hat{l}$ (see Fig. 5), the quasiparticles scatter differently when they encounter the ion with their circulation opposed to or coincident with its velocity. This simplified picture would then lead to a difference in the scattering rate ("quasiparticle pressure") across the object. The ion moving in the plane perpendicular to $\hat{l}$ thus experiences a deflecting force; the Cooper-pair angular momentum is transferred into the linear transverse momentum of the ion, which can thus be used to detect the orbital angular momentum of the condensate.

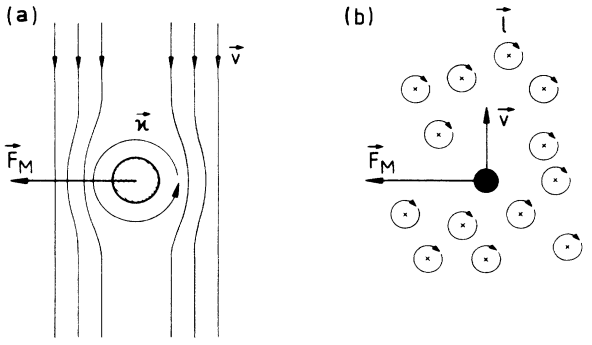

FIG. 11. Magnus force $\mathbf{F}_M$ illustrated in (a) the classical hydrodynamic situation with liquid flowing past a rotating object, and (b) the quantum-mechanical case where a nonrotating particle moves through a fluid possessing a spontaneous internal angular momentum $\hat{l}$.

When all contributions are included, we may express the velocity, Eq. (4), of the negative ion as

$$\mathbf{v} = [\mu_\parallel (\hat{l}\cdot\hat{\mathcal{E}})\hat{l} + \mu_\perp \hat{l}\times(\hat{l}\times\hat{\mathcal{E}}) + \mu_{xy}(\hat{l}\times\hat{\mathcal{E}})]\mathcal{E} \tag{47}$$

for a general orientation of $\mathcal{E}$, i.e., the driving force on ions, with respect to $\hat{l}$.

For the P phase the mobilities are plotted as functions of the corresponding energy gap in Fig. 10(b). There are no previous calculations in this phase; we have compared our result with the constant-cross-section approximation. Our calculation gives the linear mobilities

$$\frac{\mu_\parallel^P}{\mu^N} = 1 + 0.618 \frac{\Delta_P(T)}{k_B T} ,$$
$$\frac{\mu_\perp^P}{\mu^N} = 1 + 0.371 \frac{\Delta_P(T)}{k_B T} , \tag{48}$$

close to T_c; here the main discrepancy with respect to the constant-cross-section approximation is found in the parallel mobility.

The ^{3}He-A_1 phase is a mixture of normal fluid and a condensate with the spin projection $\uparrow\uparrow$; hence the scattering equation is separable in spin, and the energy-gap matrix is diagonal. Applying Eq. (5), we may express the inverse mobility in the A_1 phase through the geometric mean of the mobilities in the normal fluid and in the A phase,

$$(\mu^{A_1})^{-1} = (\tfrac{1}{2})[(\mu^A)^{-1} + (\mu^N)^{-1}] .$$

The linear approximations close to T_c may thus be written as

$$\frac{\mu_\parallel^{A_1}}{\mu^N} = 1 + 0.266 \frac{\Delta_{A_1}(T)}{k_B T} ,$$
$$\frac{\mu_\perp^{A_1}}{\mu^N} = 1 + 0.364 \frac{\Delta_{A_1}(T)}{k_B T} . \tag{49}$$

VIII. DISCUSSION

The motion of negative ions in superfluid ^{3}He is limited by collisions with superfluid quasiparticles. This is essentially a resonant-scattering problem involving several partial waves. The Lippman-Schwinger equation contains all scattering channels and virtual intermediate states. We have developed a new numerical method for solving this equation directly to obtain the scattering matrix T; this is a straightforward and physically obvious scheme, giving further insight in the nature of the resonant-scattering process.

Applying this method, we have studied and contrasted the ion mobility in two anisotropic phases, one with

Cooper pairs having $L_z \neq 0$ (^{3}He-A), the other with $L_z = 0$ (^{3}He-P); in addition to superfluid ^{3}He, these phases are also relevant for heavy-fermion superconductors, which may exhibit p-wave pairing as well. In the axisymmetric case, the polar angles θ and θ' of the initial and final quasiparticle momenta must be considered separately, while in the plane perpendicular to the symmetry axis only their relative orientation $\phi' - \phi$ counts. We perform the calculation for a grid of $\mu = \cos\theta$ and $\mu' = \cos\theta'$; the strong divergence of the density of states close to the gap edge is taken care of by employing modified Gaussian integration points.

The different topology of the energy gap in ^{3}He-A (two points on the $\hat{l}$ axis) and ^{3}He-P (a circle of nodes in the plane perpendicular to the symmetry axis) leads to the interesting observation that, even though the differential cross sections in the two phases are very similar, the transport cross sections, integrated over the allowed directions of initial and final state momenta, show qualitatively quite different behavior. In ^{3}He-A, quasibound energy levels are formed inside the energy gap; their number roughly equals the number of relevant partial waves, $p_F R$; these resonant levels are clearly seen in the cross sections. In ^{3}He-P, however, no such strong interaction between the quasiparticles and the virtual energy levels seems to exist, the quasiparticle states are more dense due to the large phase space, and only a shallow peak is observed, arising from the enhanced backscattering below the gap edge.

The negative-ion mobility may be employed to probe fundamental properties of the superfluids, such as the energy gap. Figure 12 displays $\Delta_A(T)$, which appears in the above formulae as a parameter, now extracted from the experimental data of Refs. 17 and 22, using Fig. 10(a). Owing to the respective cell geometries, the data of Ahonen *et al.*[17] are taken to represent $(\mu_\parallel^A + \mu_\perp^A)/2$, while the results of Simola *et al.*[22] represent $\mu_\perp^A$. The two sets of data coincide and we obtain a single BCS-like gap with a prefactor of 1.32 at 29 bars. Since the results of Roach *et al.*[23] are considerably above all sets of the data employed here, we have excluded them from our analysis.

The nonzero angular momentum L_z of the condensate in ^{3}He-A gives rise to a novel, quantum-mechanical deflecting force in real space, analogous to the classical Magnus force; the strength of the interaction between the ion and the quasiparticle depends on whether the angular momentum counteracts or reinforces the direction of the quasiparticle momentum (see Fig. 5 for the asymmetric differential cross section). We have evaluated this Magnus-like effect in ^{3}He-A;[21] it is a direct measure of the angular momentum of the Cooper pairs in the A phase. The predicted additional anisotropy in the mobility of negative ions, in the plane perpendicular to $\hat{l}$, has not yet been measured with equipment designed for a study of this phenomenon. Existence of a similar type of transport phenomenon, e.g., in ^{3}He-A_1 or in heavy-fermion superconductors,[7,8] would suggest pairing in states with $L_z \neq 0$.

Our calculational method can be extended to consider nonlinear motion of negative ions in ^{3}He-B, and the ionic mobility in a magnetic field, where more complicated $L_z \neq 0$ effects are expected also in the B phase. A vibrating wire in a superfluid at low enough temperatures could, in principle, be successfully treated with this approach. Ion mobility in the inhomogeneous states of superfluid ^{3}He, e.g., quantized vortices, provides an intriguing area for further research. For a detailed calculation the bulk approximation is not sufficient, but the spatial distribution of $\Delta(\hat{\mathbf{p}})$ must be included.

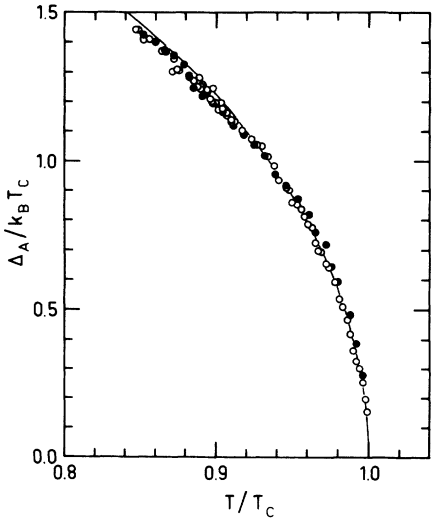

FIG. 12. Superfluid energy gap in the A phase, extracted from experimental ion mobilities employing Fig. 10(a). Measurements of Ahonen *et al.* (Ref. 17) (○) at 28.4 bars and Simola *et al.* (Ref. 22) (●) at 29.3 bars are included. The solid line represents $1.32\Delta_{BCS}(T)$ (Ref. 18).

ACKNOWLEDGMENTS

One of us (M.M.S.) is grateful to Professors Gordon A. Baym and Christopher J. Pethick for collaboration at the initial stages of this work and for their continuing interest. The latter also drew our attention to the possible anisotropy in the plane perpendicular to the symmetry axis. We want to thank the experimental groups at Helsinki, Argonne, and Lancaster for making their original data available to us, and for several useful conversations. We also thank Professor O. V. Lounasmaa for useful comments on the manuscript. Support from the Finnish Cultural Foundation and the Magnus Ehrnrooth Foundation (R.H.S.) is gratefully acknowledged; this work was supported by the Körber Stiftung (Hamburg, FRG) and by the Academy of Finland.

APPENDIX A: NUMERICAL TECHNIQUES

In the A phase, the Lippman-Schwinger equation (30) is given by

$$t_1^m(\mu',\mu)=t_N^m(\mu',\mu)+i\int_{-1}^{+1}\frac{d\mu''}{2}t_N^m(\mu',\mu'')\left[\frac{E}{[E^2-\Delta_A^2(1-\mu''^2)]^{1/2}}-1\right]t_1^m(\mu'',\mu)$$
$$+i\int_{-1}^{+1}\frac{d\mu''}{2}t_N^m(\mu',\mu'')\frac{\Delta_A(1-\mu''^2)^{1/2}}{[E^2-\Delta_A^2(1-\mu''^2)]^{1/2}}(-1)^m t_3^m(-\mu'',\mu)\ ,$$
$$t_3^m(-\mu',\mu)=-i\int_{-1}^{+1}\frac{d\mu''}{2}t_N^{m+1}(\mu',\mu'')^*\frac{\Delta_A(1-\mu''^2)^{1/2}}{[E^2-\Delta_A^2(1-\mu''^2)]^{1/2}}(-1)^m t_1^m(\mu'',\mu)$$
$$-i\int_{-1}^{+1}\frac{d\mu''}{2}t_N^{m+1}(\mu',\mu'')^*\left[\frac{E}{[E^2-\Delta_A^2(1-\mu''^2)]^{1/2}}-1\right]t_3^m(-\mu'',\mu)$$

and (A1)

$$t_2^m(\mu',-\mu)=+i\int_{-1}^{+1}\frac{d\mu''}{2}t_N^{m-1}(\mu',\mu'')\left[\frac{E}{[E^2-\Delta_A^2(1-\mu''^2)]^{1/2}}-1\right]t_2^m(\mu'',-\mu)$$
$$+i\int_{-1}^{+1}\frac{d\mu''}{2}t_N^{m-1}(\mu',\mu'')\frac{\Delta_A(1-\mu''^2)^{1/2}}{[E^2-\Delta_A^2(1-\mu''^2)]^{1/2}}(-1)^{m+1}t_4^m(-\mu'',-\mu)\ ,$$
$$t_4^m(-\mu',-\mu)=-t_N^m(\mu',\mu)^*-i\int_{-1}^{+1}\frac{d\mu''}{2}t_N^m(\mu',\mu'')^*\frac{\Delta_A(1-\mu''^2)^{1/2}}{[E^2-\Delta_A^2(1-\mu''^2)]^{1/2}}(-1)^{m+1}t_2^m(\mu'',-\mu)$$
$$-i\int_{-1}^{+1}\frac{d\mu''}{2}t_N^m(\mu',\mu'')^*\left[\frac{E}{[E^2-\Delta_A^2(1-\mu''^2)]^{1/2}}-1\right]t_4^m(-\mu'',-\mu)\ .$$

In the P phase, the corresponding equations are given by

$$t_1^m(\mu',\mu)=t_N^m(\mu',\mu)+i\int_{-1}^{+1}\frac{d\mu''}{2}t_N^m(\mu',\mu'')\left[\frac{E}{[E^2-(\Delta_P\mu'')^2]^{1/2}}-1\right]t_1^m(\mu'',\mu)$$
$$-i\int_{-1}^{+1}\frac{d\mu''}{2}t_N^m(\mu',\mu'')\frac{\Delta_P\mu''}{[E^2-(\Delta_P\mu'')^2]^{1/2}}(-1)^m t_3^m(-\mu'',\mu)\ ,$$
$$t_3^m(-\mu',\mu)=+i\int_{-1}^{+1}\frac{d\mu''}{2}t_N^m(\mu',\mu'')^*\frac{\Delta_P\mu''}{[E^2-(\Delta_P\mu'')^2]^{1/2}}(-1)^m t_1^m(\mu'',\mu)$$
$$-i\int_{-1}^{+1}\frac{d\mu''}{2}t_N^m(\mu',\mu'')^*\left[\frac{E}{[E^2-(\Delta_P\mu'')^2]^{1/2}}-1\right]t_3^m(-\mu'',\mu)$$

and (A2)

$$t_2^m(\mu',-\mu)=+i\int_{-1}^{+1}\frac{d\mu''}{2}t_N^m(\mu',\mu'')\left[\frac{E}{[E^2-(\Delta_P\mu'')^2]^{1/2}}-1\right]t_2^m(\mu'',-\mu)$$
$$-i\int_{-1}^{+1}\frac{d\mu''}{2}t_N^m(\mu',\mu'')\frac{\Delta_P\mu''}{[E^2-(\Delta_P\mu'')^2]^{1/2}}(-1)^m t_4^m(-\mu'',-\mu)\ ,$$
$$t_4^m(-\mu',-\mu)=-t_N^m(\mu',\mu)^*+i\int_{-1}^{+1}\frac{d\mu''}{2}t_N^m(\mu',\mu'')^*\frac{\Delta_P\mu''}{[E^2-(\Delta_P\mu'')^2]^{1/2}}(-1)^m t_2^m(\mu'',-\mu)$$
$$-i\int_{-1}^{+1}\frac{d\mu''}{2}t_N^m(\mu',\mu'')^*\left[\frac{E}{[E^2-(\Delta_P\mu'')^2]^{1/2}}-1\right]t_4^m(-\mu'',-\mu)\ .$$

The preceding equations express the scattering amplitudes in the four channels $\pm\hat{\mathbf{p}}\to\pm\hat{\mathbf{p}}'$, showing the correlation across the Fermi sphere of the initial- and final-state quasiparticle momenta. The $+\hat{\mathbf{p}}$ initial state amplitudes $t_1^m(\mu',\mu)$ and $t_3^m(-\mu',\mu)$ are coupled; the other pair is composed of $t_2^m(\mu',-\mu)$ and $t_4^m(-\mu',-\mu)$ for the inverse initial momentum $-\hat{\mathbf{p}}$.

When Eq. (A1) is discretized in μ'', we obtain

$$\begin{bmatrix}\delta_{fv}-\frac{i}{2}t_{N,fv}^m g_v w_v & -\frac{i}{2}t_{N,fv}^m f_v(-1)^m w_v\\ -\frac{i}{2}\left[t_{N,fv}^{m+1}\right]^* f_v(-1)^{m+1}w_v & \delta_{fv}+\frac{i}{2}(t_{N,fv}^{m+1})^* g_v w_v\end{bmatrix}\begin{bmatrix}t_{1,vi}^m & t_{2,vi}^{m+1}\\ t_{3,vi}^m & t_{4,vi}^{m+1}\end{bmatrix}=\begin{bmatrix}t_{N,fi}^m & 0\\ 0 & (t_{N,fi}^{m+1})^*\end{bmatrix}\ , \tag{A3}$$

where δ_{fv} is the Kronecker delta function, and i, v, and f indicate the initial, virtual intermediate, and final scattering states, respectively. The functions g and f (excluding $e^{i\phi}$) are given in Eqs. (37) and (38). All components are themselves $N\times N$ matrices, where N is the adjustable number of discrete values for μ, μ'', and μ' between -1 and $+1$; w_v are the weight factors at the discretization points.

When the quasiparticle energy E exceeds the maximum value of the superfluid energy gap Δ_A, the integration is performed over all possible directions, and there are no divergences; the regular Gaussian points $\xi_i^{(2n)}$ and weights $w_i^{(2n)}$ are then employed.[24] Below the gap edge, however, a limiting angle appears, shown in Fig. 13, which divides the sphere into regimes of real scattering states and those only allowed as intermediate states. The matrix equation (30) is solved for all directions, but the discretization needs to be reconsidered, as g and f now display a divergence at the limiting angle $\mu_A=(1-\hat{E}^2)^{1/2}$. In the virtual scattering state regime, $-\mu_A<\mu<\mu_A$, the regular Gaussian points are replaced by $\xi_i=\mu_A[1-(\xi_i^{(2n)})^2]$ and the weights by $w_i=2(\mu_A)^{1/2}w_i^{(2n)}$, while in the regime $|\mu|\geq\mu_A$ the grid points are given as $\xi_i=\mu_A-(1-\mu_A)(\xi_i^{(2n)})^2$ and the weights as $w_i=2(1-\mu_A)^{1/2}w_i^{(2n)}$.[24] The density of the calculation points rapidly increases when approaching the limiting angle, thus allowing an accurate description of effects due to the divergence.

The integrations of the cross sections, Eqs. (6)–(8), are done on the same grid, over real initial and final scattering states only, since these formulae feature the same singular square-root structures that cause the instabilities in the t_i^m matrices. The calculations are performed for each $m=-m_{\max}\cdots+m_{\max}$ and the A, $B^{\pm}$, and $C^{\pm}$ matrices in Appendix B are finally obtained as the sum over all values m. The procedure is analogous for the P phase.

The accuracy of the solution now depends on the density of the grid. We made the calculations at a level where the changes in the cross sections were on the order of $\frac{1}{1000}$ of the previous value when two more grid divisions were added. This required the use of $N=36$ grid points at $\hat{E}=0.1$, of which 8 were in the real scattering regime. With increasing energy, the number of points could be reduced to 24 (total)/14 (real) at $\hat{E}=0.8$–0.9, until the nearness of the gap edge required the use of 30 (total)/16–20 (real) points. Immediately above $\hat{E}=1.0$, 30 (total and real) points were still employed but at $\hat{E}>1.5$ the number could be reduced to 20. The largest complex matrices solved were thus 72×72. A symmetrization of the equations, which reduces the matrix dimensions by one half according to Ref. 6, would be useful for larger matrices which will be needed, e.g., in the solution of the equations for ^{3}He-B in the nonlinear regime.

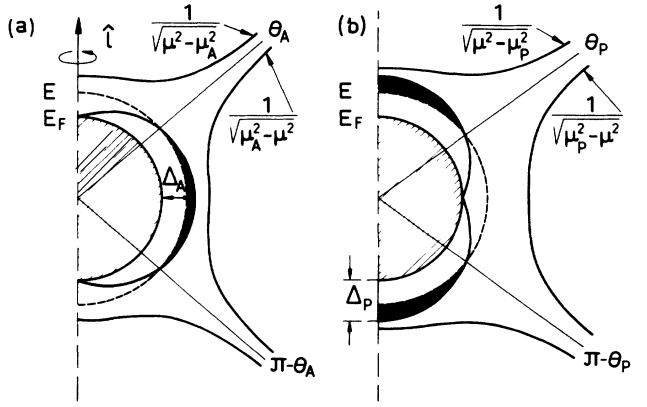

FIG. 13. For the quasiparticle energies $E<\Delta$, forbidden regimes of $\mu=\cos\theta$ appear, where no initial or final scattering states exist. These virtual intermediate states are indicated as the shaded areas below the gap edge (a) in the A phase, for $|\mu|<\mu_A=[1-(E/\Delta_A)^2]^{1/2}$ and (b) in the polar phase, for $\mu_P=E/\Delta_P<|\mu|<1$. The square-root divergences of Eqs. (8), (37), (38), (42), and (43) for $|\mu|\to\mu_A$ and $|\mu|\to\mu_P$ are also shown. The lightly shaded hemisphere marked with E_F denotes the Fermi sphere.

APPENDIX B: TECHNICAL DETAILS OF THE CROSS-SECTION CALCULATION

The averaged cross sections may be expressed employing the matrices $A(\mu',\mu)$, $B^{\pm}(\mu',\mu)$, and $C^{\pm}(\mu',\mu)$ defined in Eqs. (45):

$$\langle\sigma_{\rm tot}(E)\rangle=\int_{-1}^{1}\frac{d\mu}{2}\int_{-1}^{1}d\mu'\frac{E}{[E^2-|\Delta(\mu)|^2]^{1/2}}\frac{E}{[E^2-|\Delta(\mu')|^2]^{1/2}}A(\mu',\mu)\ , \tag{B1a}$$

$$\langle\sigma_{xx}(E)\rangle=\int_{-1}^{1}\frac{d\mu}{2}\int_{-1}^{1}d\mu'\frac{E}{[E^2-|\Delta(\mu)|^2]^{1/2}}\frac{E}{[E^2-|\Delta(\mu')|^2]^{1/2}}$$
$$\times\{(\tfrac{3}{2}-\mu^2-\tfrac{1}{2}\mu'^2)A(\mu',\mu)+\tfrac{1}{4}(1-\mu'^2)[C^+(\mu',\mu)+C^-(\mu',\mu)]$$
$$-(1-\mu^2)^{1/2}(1-\mu'^2)^{1/2}[B^+(\mu',\mu)+B^-(\mu',\mu)]\}\ , \tag{B1b}$$

$$\langle\sigma_{yy}(E)\rangle=\int_{-1}^{1}\frac{d\mu}{2}\int_{-1}^{1}d\mu'\frac{E}{[E^2-|\Delta(\mu)|^2]^{1/2}}\frac{E}{[E^2-|\Delta(\mu')|^2]^{1/2}}$$
$$\times\tfrac{1}{4}(1-\mu'^2)[2A(\mu',\mu)-C^+(\mu',\mu)-C^-(\mu',\mu)]\ , \tag{B1c}$$

$$\langle \sigma_{zz}(E)\rangle = \int_{-1}^{1}\frac{d\mu}{2}\int_{-1}^{1}d\mu' \frac{E}{[E^2-|\Delta(\mu)|^2]^{1/2}}\frac{E}{[E^2-|\Delta(\mu')|^2]^{1/2}}(\mu'-\mu)^2 A(\mu',\mu)\ , \tag{B1d}$$

$$\langle \sigma_{xy}(E)\rangle = \int_{-1}^{1}\frac{d\mu}{2}\int_{-1}^{1}d\mu' \frac{E}{[E^2-|\Delta(\mu)|^2]^{1/2}}\frac{E}{[E^2-|\Delta(\mu')|^2]^{1/2}} \times\left[-\frac{1}{2i}(1-\mu^2)^{1/2}(1-\mu'^2)^{1/2}[B^+(\mu',\mu)-B^-(\mu',\mu)] + \frac{1}{4i}(1-\mu^2)[C^+(\mu',\mu)-C^-(\mu',\mu)]\right], \tag{B1e}$$

$$\langle \sigma_{xz}(E)\rangle = \int_{-1}^{1}\frac{d\mu}{2}\int_{-1}^{1}d\mu' \frac{E}{[E^2-|\Delta(\mu)|^2]^{1/2}}\frac{E}{[E^2-|\Delta(\mu')|^2]^{1/2}} \times(\mu-\mu')\{(1-\mu^2)^{1/2}A(\mu',\mu)-\tfrac{1}{2}(1-\mu'^2)^{1/2}[B^+(\mu',\mu)+B^-(\mu',\mu)]\}\ , \tag{B1f}$$

$$\langle \sigma_{yz}(E)\rangle = \int_{-1}^{1}\frac{d\mu}{2}\int_{-1}^{1}d\mu' \frac{E}{[E^2-|\Delta(\mu)|^2]^{1/2}}\frac{E}{[E^2-|\Delta(\mu')|^2]^{1/2}} \times\left[-\frac{1}{2i}\right](\mu-\mu')(1-\mu'^2)^{1/2}[B^+(\mu',\mu)-B^-(\mu',\mu)]\ , \tag{B1g}$$

for $E>\Delta$, while for $E<\Delta$ the integrations must be limited to the regions of real initial and final scattering states as discussed in Sec. III, reducing the phase space for $\langle |t_{\hat{p}'\hat{p}}(E)|^2\rangle$.

In the A phase, Eq. (34) is found to become

$$\begin{aligned}\langle |t_{\hat{p}'\hat{p}}|^2\rangle_A = \frac{1}{2}\left[\frac{1}{\pi N(0)}\right]^2 \sum_{m=-\infty}^{\infty}\sum_{m'=-\infty}^{\infty} e^{-i(m'-m)(\phi'-\phi)} \\ \times\Bigg[\left[t_1^m(\mu',\mu)^*-\frac{(1-\mu^2)^{1/2}}{\hat{E}}e^{-i(\phi'-\phi)}(-1)^m t_2^m(\mu',-\mu)^*\right] \\ \times\left[t_1^{m'}(\mu',\mu)-\frac{(1-\mu'^2)^{1/2}}{\hat{E}}(-1)^{m'+1}t_3^{m'}(-\mu',\mu)\right] \\ +\left[(-1)^m t_2^m(\mu',-\mu)^*-\frac{(1-\mu^2)^{1/2}}{\hat{E}}e^{i(\phi'-\phi)}t_1^m(\mu',\mu)^*\right] \\ \times\left[(-1)^{m'}t_2^{m'}(\mu',-\mu)-\frac{(1-\mu'^2)^{1/2}}{\hat{E}}t_4^{m'}(-\mu',-\mu)\right] \\ +\left[(-1)^{m+1}t_3^m(-\mu',\mu)^*-\frac{(1-\mu^2)^{1/2}}{\hat{E}}e^{-i(\phi'-\phi)}t_4^m(-\mu',-\mu)^*\right] \\ \times\left[(-1)^{m'+1}t_3^{m'}(-\mu',\mu)-\frac{(1-\mu'^2)^{1/2}}{\hat{E}}t_1^{m'}(\mu',\mu)\right] \\ +\left[t_4^m(-\mu',-\mu)^*-\frac{(1-\mu^2)^{1/2}}{\hat{E}}e^{i(\phi'-\phi)}(-1)^{m+1}t_3^m(-\mu',\mu)^*\right] \\ \times\left[t_4^{m'}(-\mu',-\mu)-\frac{(1-\mu'^2)^{1/2}}{\hat{E}}(-1)^{m'}t_2^{m'}(\mu',-\mu)\right]\Bigg]\ .\end{aligned} \tag{B2}$$

The sum over the partial wave projections m may be restricted to values for which the phase shifts are appreciable, i.e., only for $m=-m_{\max}\ldots+m_{\max}$, where $m_{\max}$ is on the order of $p_F R$; for the experimentally relevant value $p_F R=8.45$ we included $m_{\max}=13$ partial waves. This does not cause considerable errors, because the phase shifts δ_l in the normal phase scattering matrix components, Eq. (22), vanish rapidly when $|m|$ exceeds $p_F R$.[6] In the P phase we ob-

tain the effective squared T-matrix element as

$$\langle |t_{\hat{\mathbf{p}}'\hat{\mathbf{p}}}|^2 \rangle_P = \frac{1}{2}\left[\frac{1}{\pi N(0)}\right]^2 \sum_{m=-\infty}^{\infty}\sum_{m'=-\infty}^{\infty} e^{-i(m'-m)(\phi'-\phi)} \left[\left[t_1^m(\mu',\mu)^* - \frac{\mu}{\hat{E}}(-1)^m t_2^m(\mu',-\mu)^*\right]\right.$$
$$\times\left[t_1^{m'}(\mu',\mu) - \frac{\mu'}{\hat{E}}(-1)^{m'} t_3^{m'}(-\mu',\mu)\right]$$
$$+\left[(-1)^m t_2^m(\mu',-\mu)^* - \frac{\mu}{\hat{E}} t_1^m(\mu',\mu)^*\right]$$
$$\times\left[(-1)^{m'} t_2^{m'}(\mu',-\mu) - \frac{\mu'}{\hat{E}} t_4^{m'}(-\mu',-\mu)\right]$$
$$+\left[(-1)^m t_3^m(-\mu',\mu)^* - \frac{\mu}{\hat{E}} t_4^m(-\mu',-\mu)^*\right]$$
$$\times\left[(-1)^{m'} t_3^{m'}(-\mu',\mu) - \frac{\mu'}{\hat{E}} t_1^{m'}(\mu',\mu)\right]$$
$$+\left[t_4^m(-\mu',-\mu)^* - \frac{\mu}{\hat{E}}(-1)^m t_3^m(-\mu',\mu)^*\right]$$
$$\left.\times\left[t_4^{m'}(-\mu',-\mu) - \frac{\mu'}{\hat{E}}(-1)^{m'} t_2^{m'}(\mu',-\mu)\right]\right]. \tag{B3}$$

We perform the ϕ-integration of the T-matrix element to find the matrices $A(\mu',\mu)$, $B^{\pm}(\mu',\mu)$, and $C^{\pm}(\mu',\mu)$, Eq. (45). For example, in ^{3}He-A the terms responsible for the intrinsic Magnus effect are

$$B_A^+(\mu',\mu) = \pi \sum_{m=-\infty}^{\infty}\left[\left[t_1^{m-1}(\mu',\mu)^* - \frac{(1-\mu^2)^{1/2}}{\hat{E}}(-1)^m t_2^m(\mu',-\mu)^*\right]\right.$$
$$\times\left[t_1^m(\mu',\mu) - \frac{(1-\mu'^2)^{1/2}}{\hat{E}}(-1)^{m+1} t_3^m(-\mu',\mu)\right]$$
$$+\left[(-1)^m t_2^m(\mu',-\mu)^* - \frac{(1-\mu^2)^{1/2}}{\hat{E}} t_1^{m-1}(\mu',\mu)^*\right]$$
$$\times\left[(-1)^{m+1} t_2^{m+1}(\mu',-\mu) - \frac{(1-\mu'^2)^{1/2}}{\hat{E}} t_4^{m+1}(-\mu',-\mu)\right]$$
$$+\left[(-1)^m t_3^{m-1}(-\mu',\mu)^* - \frac{(1-\mu^2)^{1/2}}{\hat{E}} t_4^m(-\mu',-\mu)^*\right]$$
$$\times\left[(-1)^{m+1} t_3^m(-\mu',\mu) - \frac{(1-\mu'^2)^{1/2}}{\hat{E}} t_1^m(\mu',\mu)\right]$$
$$+\left[t_4^m(-\mu',-\mu)^* - \frac{(1-\mu^2)^{1/2}}{\hat{E}}(-1)^m t_3^{m-1}(-\mu',\mu)^*\right]$$
$$\left.\times\left[t_4^{m+1}(-\mu',-\mu) - \frac{(1-\mu'^2)^{1/2}}{\hat{E}}(-1)^{m+1} t_2^{m+1}(\mu',-\mu)\right]\right], \tag{B4}$$

and

$$
\begin{aligned}
C_A^+(\mu',\mu)=\pi \sum_{m=-\infty}^{\infty} \Bigg[& \left[t_1^{m-2}(\mu',\mu)^* - \frac{(1-\mu^2)^{1/2}}{\hat{E}}(-1)^{m+1} t_2^{m-1}(\mu',-\mu)^* \right] \\
& \times \left[t_1^{m}(\mu',\mu) - \frac{(1-\mu'^2)^{1/2}}{\hat{E}}(-1)^{m+1} t_3^{m}(-\mu',\mu) \right] \\
& + \left[(-1)^{m+1} t_2^{m-1}(\mu',-\mu)^* - \frac{(1-\mu^2)^{1/2}}{\hat{E}} t_1^{m-2}(\mu',\mu)^* \right] \\
& \times \left[(-1)^{m+1} t_2^{m+1}(\mu',-\mu) - \frac{(1-\mu'^2)^{1/2}}{\hat{E}} t_4^{m+1}(-\mu',-\mu) \right] \\
& + \left[(-1)^{m+1} t_3^{m-2}(-\mu',\mu)^* - \frac{(1-\mu^2)^{1/2}}{\hat{E}} t_4^{m-1}(-\mu',-\mu)^* \right] \\
& \times \left[(-1)^{m+1} t_3^{m}(-\mu',\mu) - \frac{(1-\mu'^2)^{1/2}}{\hat{E}} t_1^{m}(\mu',\mu) \right] \\
& + \left[t_4^{m-1}(-\mu',-\mu)^* - \frac{(1-\mu^2)^{1/2}}{\hat{E}}(-1)^{m+1} t_3^{m-2}(-\mu',\mu)^* \right] \\
& \times \left[t_4^{m+1}(-\mu',-\mu) - \frac{(1-\mu'^2)^{1/2}}{\hat{E}}(-1)^{m+1} t_2^{m+1}(\mu',-\mu) \right] \Bigg] . \qquad \text{(B5)}
\end{aligned}
$$

In the phase ^{3}He-P, the expressions have been derived in an analogous way.

The resonance between the adjacent partial waves is obvious from the preceding formulae which are mixtures of projections for $m-2,\ldots,m+2$. The asymmetry in the plane perpendicular to $\hat{l}$ in ^{3}He-A and the symmetry in the polar phase can also be seen in these equations. Since the symmetries of the T_N matrix in the normal phase are transmitted to the P phase, giving $t_i^{-m}=t_i^m$, the changing sign in the overall multiplication factor, $\exp[-i(m'-m)(\phi'-\phi)]$, does not affect the sums over m' and m. There are no other elements sensitive to the relative directions of the incident and scattering quasiparticles in the plane perpendicular to the symmetry axis, and the differential scattering cross section is symmetric about this plane. In the A phase, however, the amplitudes t_i^m loose their symmetry under reversal of the sign of m and, moreover, extra factors $\exp[i(\phi'-\phi)]$ are found inside the square brackets, destroying the reflection symmetry. This gives rise to the purely quantum-mechanical intrinsic Magnus effect analogous to the classical Magnus force.[21]

[1] C. G. Kuper, Phys. Rev. **122**, 1007 (1961).

[2] P. Muzikar, J. Phys. (Paris) Colloq. **39**, C6-53 (1978); A. L. Fetter, J. A. Sauls, and D. L. Stein, Phys. Rev. B **28**, 5061 (1983); M. M. Salomaa and G. E. Volovik, Phys. Rev. Lett. **54**, 2127 (1985).

[3] Larger objects moving in superfluid ^{3}He could generate topological excitations, such as vortex rings or particlelike solitons.

[4] R. M. Bowley, J. Phys. C **9**, L151 (1976); **10**, 4033 (1977).

[5] G. Baym, C. J. Pethick, and M. M. Salomaa, Phys. Rev. Lett. **38**, 845 (1977); J. Low Temp. Phys. **36**, 431 (1979).

[6] M. Salomaa, C. J. Pethick, and G. Baym, J. Low Temp. Phys. **40**, 297 (1980).

[7] C. J. Pethick and D. Pines, Phys. Rev. Lett. **57**, 118 (1986); H. R. Ott, E. Felder, C. Bruder, and T. M. Rice, Europhys. Lett. **3**, 1123 (1987).

[8] B. Arfi and C. J. Pethick, Phys. Rev. B **38**, 2312 (1988).

[9] M. M. Salomaa and G. E. Volovik, Rev. Mod. Phys. **59**, 533 (1987).

[10] J. Bardeen, L. N. Cooper, and J. R. Schrieffer, Phys. Rev. **108**, 1175 (1957).

[11] P. W. Anderson and P. Morel, Phys. Rev. **123**, 1911 (1961); P. W. Anderson and W. F. Brinkman, Phys. Rev. Lett. **30**, 1108 (1973).

[12] R. Abe and K. Aizu, Phys. Rev. **123**, 10 (1961); R. C. Clark, Proc. Phys. Soc. London **82**, 785 (1963); G. T. Schappert, Phys. Rev. **168**, 162 (1968); H. Winter, Z. Phys. **221**, 186 (1969); L. Kramer, Phys. Rev. A **1**, 1517 (1970).

[13] A. C. Anderson, M. Kuchnir, and J. C. Wheatley, Phys. Rev. **168**, 261 (1968); M. Kuchnir, P. R. Roach, and J. B. Ketterson, Phys. Rev. A **2**, 262 (1970); P. V. E. McClintock, J. Low Temp. Phys. **11**, 277 (1973).

[14] B. D. Josephson and J. Lekner, Phys. Rev. Lett. **23**, 111 (1969).

[15] T. Soda, Prog. Theor. Phys. **58**, 1096 (1977).

[16] D. J. Bromley, Bull. Am. Phys. Soc. **23**, 50(A) (1978).

[17] A. I. Ahonen, J. Kokko, O. V. Lounasmaa, M. A. Paalanen, R. C. Richardson, W. Schoepe, and Y. Takano, Phys. Rev. Lett. **37**, 511 (1976); A. I. Ahonen, J. Kokko, M. A. Paalanen, R. C. Richardson, W. Schoepe, and Y. Takano, J. Low Temp. Phys. **30**, 205 (1978).

[18] R. H. Salmelin and M. M. Salomaa, J. Phys. C **20**, L681

(1987).
[19]R. H. Salmelin and M. M. Salomaa, J. Phys. C **20**, L688 (1987).
[20]D. Rainer and M. Vuorio, J. Phys. C **10**, 3093 (1977).
[21]R. H. Salmelin, M. M. Salomaa, and V. P. Mineev, Phys. Rev. Lett. **63**, 868 (1989).
[22]J. T. Simola, K. K. Nummila, A. Hirai, J. S. Korhonen, W. Schoepe, and L. Skrbek, Phys. Rev. Lett. **57**, 1923 (1986); J. T. Simola, K. K. Nummila, L. Skrbek, and J. S. Korhonen, Cryogenics **27**, 391 (1987).
[23]P. D. Roach, J. B. Ketterson, and P. R. Roach, Phys. Rev. Lett. **39**, 626 (1977).
[24]P. J. Davis and I. Polonsky, in *Handbook of Mathematical Functions,* edited by M. Abramovitz and I. A. Stegun (Dover, New York, 1972), Chap. 25.

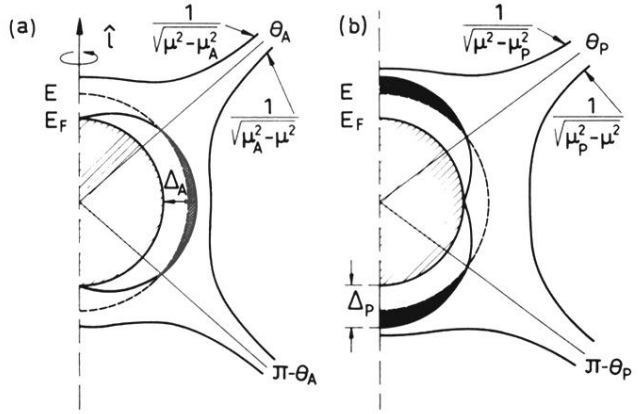

FIG. 13. For the quasiparticle energies $E<\Delta$, forbidden regimes of $\mu=\cos\theta$ appear, where no initial or final scattering states exist. These virtual intermediate states are indicated as the shaded areas below the gap edge (a) in the A phase, for $|\mu|<\mu_A=[1-(E/\Delta_A)^2]^{1/2}$ and (b) in the polar phase, for $\mu_P=E/\Delta_P<|\mu|<1$. The square-root divergences of Eqs. (8), (37), (38), (42), and (43) for $|\mu|\rightarrow\mu_A$ and $|\mu|\rightarrow\mu_P$ are also shown. The lightly shaded hemisphere marked with E_F denotes the Fermi sphere.

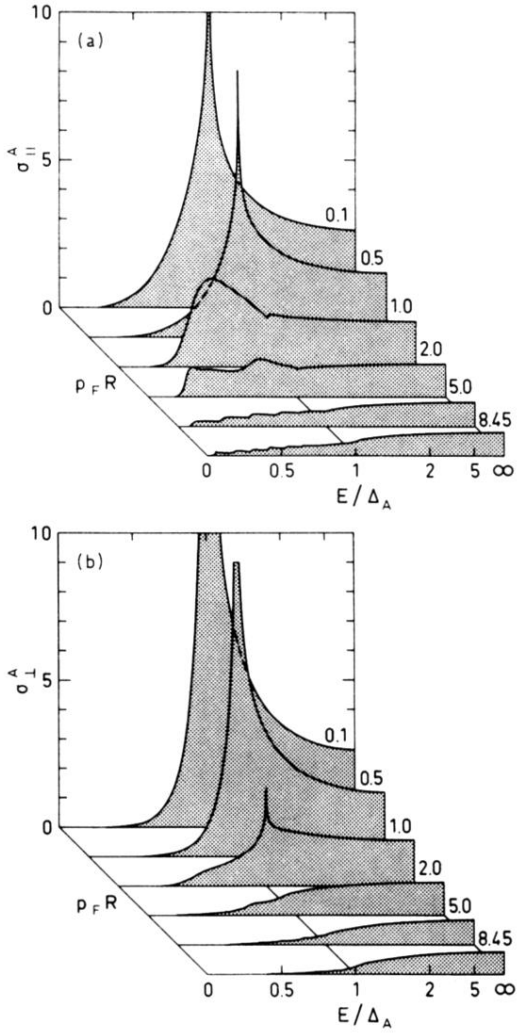

FIG. 6. Transport cross section of the quasiparticle-negative-ion scattering (a) along $\hat{l}$ and (b) in the plane perpendicular to $\hat{l}$ in ^{3}He-A in units of πR^2, plotted vs quasiparticle energy for several values of the pressure-dependent impact parameter $p_F R$, indicated on the graphs.

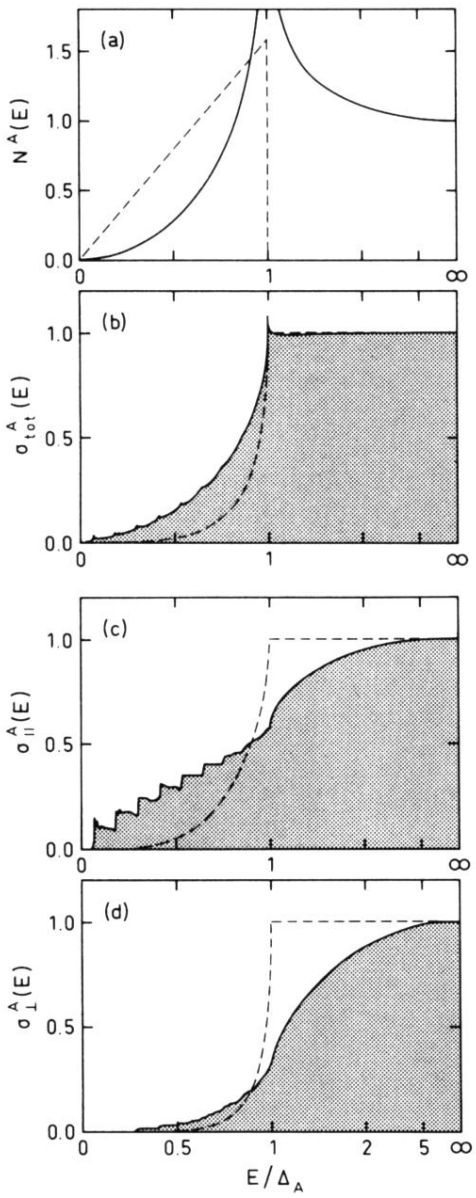

FIG. 8. Density of quasiparticle states in ^{3}He-A is featured in (a); the dashed curve is the real part while the solid curve indicates the imaginary part. In (b) through (d) the total scattering cross section and the transport cross sections along $\hat{l}$ and in the plane perpendicular to it, respectively, are illustrated for $p_F R = 8.45$, corresponding to a pressure of 29 bars, in units of the normal-state value. The stepwise structure arises from the resonant energy levels within the superfluid gap, depicted in Fig. 7.

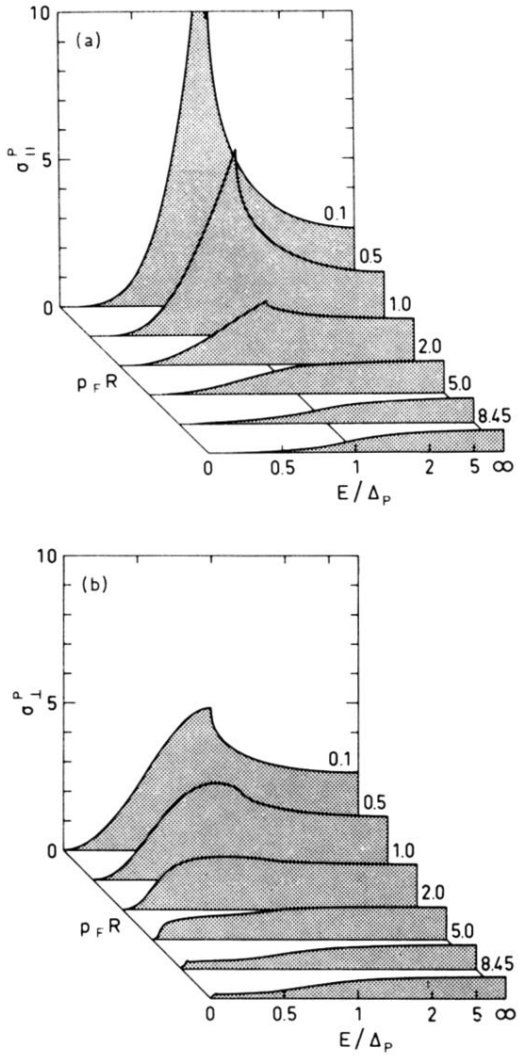

FIG. 9. Transport cross section of the quasiparticle-negative-ion scattering (a) along the symmetry axis in ^{3}He-P and (b) perpendicular to it in units of πR^2, plotted vs quasiparticle energy for several values of the impact parameter $p_F R$.